

Quantifying the Effects of Horizontal Grid Length and Parameterized Convection on the Degree of Convective Organization Using a Metric of the Potential for Convective Interaction

B. A. WHITE^a

Atmospheric, Oceanic and Planetary Physics, University of Oxford, Oxford, United Kingdom

A. M. BUCHANAN

Department of Engineering Science, University of Oxford, Oxford, United Kingdom

C. E. BIRCH

Met Office Leeds, and School of Earth and Environment, University of Leeds, Leeds, United Kingdom

P. STIER

Atmospheric, Oceanic and Planetary Physics, University of Oxford, Oxford, United Kingdom

K. J. PEARSON

Department of Meteorology, University of Reading, Reading, United Kingdom

(Manuscript received 24 October 2016, in final form 29 September 2017)

ABSTRACT

The organization of deep convection and its misrepresentation in many global models is the focus of much current interest. A new method is presented for quantifying convective organization based on the identification of convective objects and subsequent derivation of object numbers, areas, and separation distances to describe the degree of convective organization. These parameters are combined into a “convection organization potential” based on the physical principle of an interaction potential between pairs of convective objects. This technique is applied to simulated and observed fields of outgoing longwave radiation (OLR) over the West African monsoon region using data from Met Office Unified Model simulations and satellite observations made by the Geostationary Earth Radiation Budget (GERB) instrument. The method is evaluated by using it to quantify differences between models with different horizontal grid lengths and representations of convection. Distributions of OLR, precipitation and organization parameters, the diurnal cycle of convection, and relationships between the meteorology in different states of organization are compared. Switching from a configuration with parameterized convection to one that allows the model to resolve convective processes at the model grid scale is the leading-order factor improving some aspects of model performance, while increased model resolution is the dominant factor for others. However, no single model configuration performs best compared to observations, indicating underlying deficiencies in both model scaling and process understanding.

1. Introduction

Convection transports moisture, momentum, heat, and aerosols through the troposphere, so the variability of convection is a major driver of global weather and climate. Convection is observed to organize across a wide range of scales in both the tropics and midlatitudes, from the few kilometers and hours associated with individual cloud systems, through the mesoscale of squall lines and cloud

^a Denotes content that is immediately available upon publication as open access.

^a Current affiliation: School of Earth, Atmosphere and Environment, Monash University, Melbourne, Victoria, Australia.

Corresponding author: B. A. White, bethan.white@monash.edu

clusters, to the synoptic scale of tropical cyclones (Houze and Betts 1981; Houze et al. 1989; Nesbitt et al. 2000). Additionally, the diurnal cycle of convection has an important role in the triggering and control of these systems. However, the processes responsible for convective organization, and the interactions between spatiotemporal scales of convection, are still poorly understood, and global and limited-area models (LAMs) often fail to represent organized convection.

Idealized simulations performed over fixed sea surface temperatures (SST) in radiative–convective equilibrium (RCE) have found that initially random tropical convective activity self-aggregates into clusters (e.g., Tompkins 2001; Bretherton et al. 2005). However, over land surfaces (with different heat capacity compared to the ocean and with surface inhomogeneities introducing much stronger spatiotemporal variability to the forcing of convection compared to over the ocean surface) deep convection is also frequently observed to organize into larger systems such as mesoscale convective systems (MCSs) and mesoscale convective complexes (MCCs) (Maddox 1983; Cotton et al. 1983; Laing and Fritsch 1997). Factors and processes leading to the organization of convection can occur both on the large scale, such as SST gradients (Zhang 1993) and large-scale vertical wind shear (Rotunno et al. 1988; LeMone et al. 1998), and from local variations such as wind-sensitive surface fluxes (Tompkins and Craig 1998), increased convergence by cloud–radiation interactions (Sherwood 1999), and cold pools generated by convective downdrafts (e.g., Charba 1974; Simpson 1980; Thorpe et al. 1982; Fovell and Tan 1998). Convective organization has a significant effect on the vertical transport of heat, moisture, and momentum (Moncrieff and Klinker 1997).

The resolution of most current global models is still too coarse to resolve convective clouds (or even cloud systems), especially in climate rather than weather simulations, and thus convection is parameterized in such models. It is widely acknowledged that convection parameterizations fail to capture many observed features of convection: they tend to overpredict light rainfall, underpredict heavy rainfall, and produce a daily precipitation maximum that occurs too early (e.g., Randall et al. 2003; Dai and Trenberth 2004; Yang and Slingo 2001; Dai 2006; Guichard et al. 2010; Stephens et al. 2010; Dirmeyer et al. 2012). This problem is not restricted to global models: Marsham et al. (2013) found biases in a LAM with parameterized convection to resemble those in a global operational model, Holloway et al. (2013) found that high-resolution simulations using parameterized convection failed to reproduce a good Madden–Julian oscillation (MJO), and Taylor et al. (2013) found that the sign of soil moisture–precipitation

feedback in a LAM simulation with parameterized convection was opposite to that in simulations using no convection scheme. Models with permitted convection (where the horizontal resolution is sufficient to explicitly represent convective processes) have been shown to represent the West African monsoon more realistically than those with parameterized convection, through combined effects on latent heating, radiative heating, and cold outflow from storms (Marsham et al. 2011, 2013). Similarly, models using convection parameterizations have been shown to fail to produce realistic boundary layer convergence associated with convection initiation (Birch et al. 2014a).

In recent years, continuously increasing computational resources have allowed high-resolution, convection-permitting, large-domain (even, in some cases, global; Miura et al. 2007) simulations to be performed. Both factors are often changed simultaneously, going from coarser-resolution simulations with parameterized convection to finer-resolution simulations with permitted convection. Models with finer resolutions that are able to resolve convective processes explicitly have been shown to have improved diurnal cycles of convection (Guichard et al. 2004). However, studies have shown that the leading-order factor responsible for improved simulations at finer resolutions is the change in the representation of convection rather than just the increased model resolution (Pohl and Douville 2011; Dirmeyer et al. 2012; Holloway et al. 2013; Marsham et al. 2013; Pearson et al. 2013; Taylor et al. 2013; Birch et al. 2015). Nevertheless, convection-permitting simulations often overpredict the amount and strength of rainfall (Weisman et al. 1997; Holloway et al. 2012; Marsham et al. 2013), and the problem does not appear to improve as the limit of today’s model resolutions is approached: comparisons of convection-permitting simulations of convective storms from grid lengths of 1500 to 100 m against radar observations have shown that while the width of individual storms converges with increasing model resolution, storm structures at the highest resolutions are too narrow and intense (Stein et al. 2014; Hanley et al. 2015).

In addition to their limited ability to represent the diurnal cycle of convection and other convective processes (e.g., boundary layer convergence and features of the West African monsoon; Marsham et al. 2013; Birch et al. 2014b), models with convection parameterizations are frequently unable to represent organized convection. Convective organization is seen to have a strong impact on the large-scale state of the atmosphere, with states of higher organization associated with drier mean states both in models (Held et al. 1993; Tompkins 2001; Bretherton et al. 2005; Nolan et al. 2007) and

observations (Tobin et al. 2012, 2013). Thus, the missing representation of organized convection in global models may have significant implications for climate sensitivity (Tobin et al. 2013; Bony et al. 2015; Mauritsen and Stevens 2015) and the development of convection parameterization has seen particular interest in this topic recently. New parameterization approaches have been proposed, such as those that describe competing cloud types with the aim of describing a self-organized system (Nober and Graf 2005); schemes that include a prognostic variable for organization (Mapes and Neale 2011); turbulence closure schemes that can be used to unify the parameterization of shallow convection, resolved clouds, and the planetary boundary layer [e.g., Cloud Layers Unified by Binormals (CLUBB); Guo et al. 2015]; “hybrid” strategies that parameterize convective cloud but allow mesoscale organization to be represented by explicit circulations (Moncrieff and Liu 2006); and so-called super-parameterizations, which embed a 2D cloud-resolving model in each global model grid box (e.g., Grabowski 2001).

A few studies have devised methods of quantifying convective organization in order to compare the degree of organization in different models and across different observed atmospheric states. Wing and Cronin (2016) analyzed self-aggregation of convection in cloud-resolving RCE simulations by using column relative humidity, or saturation fraction (the ratio of precipitable water to the saturation water path), as a metric to diagnose aggregation. In global RCE simulations, Coppin and Bony (2015) used the fractional area of the globe covered by midtropospheric large-scale subsidence (termed the “subsiding fraction” by those authors) as a quantitative measure of convective aggregation. However, both of these approaches require analysis of 3D model fields to diagnose aggregation, which can be both expensive and can also be applied only to simulations, where such fields may not be available in observations of Earth’s atmosphere.

Seifert and Heus (2013) discuss different methods that can be applied to identify and quantify cloud field organization in large-eddy simulations. They conclude that Hovmöller diagrams are a simple tool to detect cloud field organization but have the disadvantage that their character depends on the choice of averaging direction, and it is difficult to quantify organization from such diagrams. Similarly, Fourier analysis of total water mixing ratio can be used to identify the growth of variance from small- to large-scale structures, but still cannot quantify the mode of organization (i.e., whether the cloud fields are regular, random, or clustered) (Seifert and Heus 2013). The approach used by Arnold and Randall (2015) of identifying an aggregated convective

state in global simulations as one in which the distribution of column water vapor is bimodal, with two distinct local maxima, suffers the same limitation. Using a metric of the deviation to the nearest neighbor cumulative distribution function (NNCDF), as described by Weger et al. (1992) and applied by Nair et al. (1998), Seifert and Heus (2013) performed object-based identification and tracking of cloud liquid water path (Heus and Seifert 2013) and analyze convective organization. Other authors have devised object-based techniques to identify convective organization. Birch et al. (2014a) used a measure of fractal dimension to quantify differences between convective features. Using an object-based technique, Tobin et al. (2012) developed the simple convective aggregation index (SCAI), a diagnostic quantity formed from the number of convective objects in a scene and the geometrical mean distance between the object centers of mass, while the later study of Tobin et al. (2013) used only the number of convective objects to identify aggregation. SCAI has since been used to quantify and compare convective aggregation in studies of simulated (Holloway 2017) and observed (Stein et al. 2017) convection.

Tobin et al. (2012) define SCAI for a given domain as follows:

$$\text{SCAI} = \frac{N}{N_{\max}} \frac{D_0}{L} \times 1000, \quad (1)$$

where N is the number of convective objects, N_{\max} is the maximum possible number of objects in the domain (equal to half the number of pixels or model grid points in the domain), L is the length scale of the domain, and D_0 is the geometric mean distance between the centroids of the convective objects. SCAI therefore increases both with the number of convective objects and with the mean distance D_0 and is interpreted by Tobin et al. (2012) as “the ratio of the degree of convective ‘disaggregation’ to a potential maximal disaggregation, expressed per thousand” (p. 6890). More aggregated scenes are classified by lower SCAI values, while disaggregated scenes are classified by higher SCAI values.

Although clearly shown to be a useful diagnostic quantity, the SCAI metric has some limitations. First, SCAI considers only the number of convective objects in a given domain at a given time and the geometrical mean distance between object centroids (a measure of the “clumping” of the objects). Thus, SCAI is totally insensitive to object size; that is, SCAI values will be the same in scenes with the same number of objects, each with the same centroids, but in which the objects have different sizes. SCAI must also be scaled by the “characteristic length scale” of the domain, along with the potential maximum number of objects in the domain.

These scalings mean that SCAI cannot easily be used to compare domains of very different sizes and resolutions or with very different numbers of total objects.

No metrics thus far proposed to quantify convective organization have considered the areas of convective objects alongside the numbers and spatial arrangement of objects. [Zhu et al. \(1992\)](#) performed a detailed analysis of observed cumulus cloud field spatial distributions based upon Landsat, Advanced Very High Resolution Radiometer (AVHRR), and Skylab data and found that large clouds affect the growth of other large clouds nearby; that is, the relative size of convective objects can influence and impact the development and size of other objects. It is also known that, through cold pool interactions, cloud size and proximity increase the potential for organization and therefore growth of the size of the cloud system (e.g., [Feng et al. 2015](#)). With this in mind, we develop a new and complementary metric to diagnose convective organization. Our new metric is able to account for the areas of convective objects and is physically motivated by the potential for convective systems to interact in 2D. While we acknowledge the importance of the properties of the larger-scale environment (e.g., wind shear, humidity) on the development and interaction of convection, we choose to focus here on the interaction of individual systems on time scales of single cloud system life cycles.

Our metric also improves on some of the limitations of SCAI described above. We apply this metric to data from simulations from the Cascade project, a consortium project designed to study organized tropical convection using large-domain cloud-system resolving simulations over a range of model resolutions and representations of convection. The Cascade simulations and satellite observations used in this paper are described in [section 2](#). Cascade allowed studies of the effects of model resolution and convection representation on the MJO ([Holloway et al. 2013](#)), precipitation distributions over the tropical ocean ([Holloway et al. 2012](#)), and the diurnal cycle of convection over West Africa ([Pearson et al. 2010, 2013](#)) and over the Maritime Continent ([Love et al. 2011](#)). Previous studies of convective organization have focused on oceanic tropical convection (e.g., [Bretherton et al. 2005](#); [Tobin et al. 2012, 2013](#)); however, we present an analysis of convective organization over tropical land focusing on the West African Cascade region also studied by [Pearson et al. \(2010, 2013\)](#). This is nonequilibrium convection over a strongly heterogeneous diurnally forced land surface, rather than self-aggregating convection in an RCE environment [as is the focus of, e.g., [Tompkins \(2001\)](#) and [Bretherton et al. \(2005\)](#)]. Our new metric (referred to as an “organization potential”)

is described in [section 3](#), along with details of the methods used to identify convective objects. In [section 4](#) we analyze the Cascade simulations in terms of our organization metric and compare the results against satellite observations of cloud and precipitation. Specifically, we use our metric to quantify differences in convective organization between model resolutions and between simulations with and without a convection parameterization.

2. Data

As part of the Cascade project, LAM simulations were performed over West Africa using the Met Office Unified Model (UM) with horizontal grid lengths of 12, 4, and 1.5 km with no convection parameterization (referred to herein as 12kmExp, 4kmExp, and 1.5kmExp, respectively) and at 12-km grid length using a mass flux parameterization (12kmParam). The model configurations were designed to be as similar as possible except for their representations of convection. The same radiation and boundary layer mixing parameterizations were used in all model configurations, although some of the parameters and settings in these schemes differ between configurations. [Pearson et al. \(2013\)](#) give a full description of the model configurations. We present data from 9 days of simulation initialized using analyses from the European Centre for Medium-Range Weather Forecasts (ECMWF) at 0000 UTC 26 July 2006. The 9-day sample is sufficient to reach a state where the results robustly represent the model performance (see [appendix A](#)). Boundary forcing from ECMWF analyses was every 6 h for 12kmParam and 12kmExp. The high-resolution simulations without parameterized convection were nested one way within each other: the 4kmExp simulation was forced at its boundaries every 30 min from 12kmParam and the 1.5kmExp simulation was forced at its boundaries every 15 min by 4kmExp. Further details and a figure of the nested computational domains used in the permitted-convection simulations can be found in [Pearson et al. \(2013\)](#).

Observations of OLR in this analysis are provided from the Geostationary Earth Radiation Budget (GERB; [Harries et al. 2005](#)) instrument, a broadband radiometer measuring thermal radiation on the geostationary *Meteosat-8* satellite. The satellite is positioned over the equator with a field of view covering all of the African continent. The nadir resolution of GERB is approximately 40 km—relatively coarse compared to the resolution of the Cascade models. We therefore use a hybrid GERB product (NRT V003 ARCH) that includes information from the Spinning Enhanced Visible and Infrared Imager (SEVIRI), also on *Meteosat-8*,

to produce high-resolution OLR measurements at approximately 10-km resolution. The product is described in Dewitte et al. (2008), where it is termed Standard High-Resolution Image (SHI). For clarity, we refer to this product throughout the rest of this paper as GERB-SEVIRI. This product was first used to study the effect of Saharan dust on the atmospheric radiation balance (Slingo et al. 2006) and has since been used in two other Cascade studies (Pearson et al. 2010, 2013). Observations of precipitation were provided by the Tropical Rainfall Measuring Mission (TRMM; Huffman et al. 2007) 3B42 product, a gridded, merged 3-hourly mean multisatellite precipitation analysis estimate at 0.25° spatial resolution. Data from the satellites were selected at the closest times matching the model outputs.

Data from each of the models were first coarse grained to the resolution of the GERB-SEVIRI data. The model and satellite data were then subsectioned onto a domain of $4^\circ\text{--}23^\circ\text{N}$, $17^\circ\text{W}\text{--}13^\circ\text{E}$ (a region smaller than that of the smallest model domain) in order to compare data over identical geographical areas and in order to remove any regions that may be subject to the influence of model boundary effects. The convective-object identification algorithm described below in section 3a was run on the OLR field from each of the datasets. The organization parameters were then calculated for each output time, giving a time series of parameters for each dataset. Where model data are compared directly against the TRMM-3B42 product, the precipitation fields from the models are coarsened to the 0.25° resolution and 3-hourly mean of the TRMM-3B42 dataset.

3. Methods

a. Identification of convective objects

We identify convective objects from outgoing long-wave radiation (OLR) fields from the models and observations. Studies often threshold broadband (e.g., OLR) or narrowband (e.g., brightness temperatures) fields to identify regions of deep convection. Narrowband brightness temperature thresholds used in the literature cover a wide range of values, from 188 to 267 K to detect cloudy areas (Mapes and Houze 1993), 215 K for deep convective cloud and 267 K for anvil regions (Fu et al. 1990), and a relatively warm threshold of 235 K (Roca et al. 2017) or 240 K (Roca and Ramanathan 2000; Tobin et al. 2012, 2013) to identify broad convective systems rather than convective cores. Values used to detect deep convection from broadband OLR fields range from 240 W m^{-2} (Fu et al. 1990), 235 W m^{-2} (Futyuan and Del Genio 2007), 210 W m^{-2} (Inoue et al.

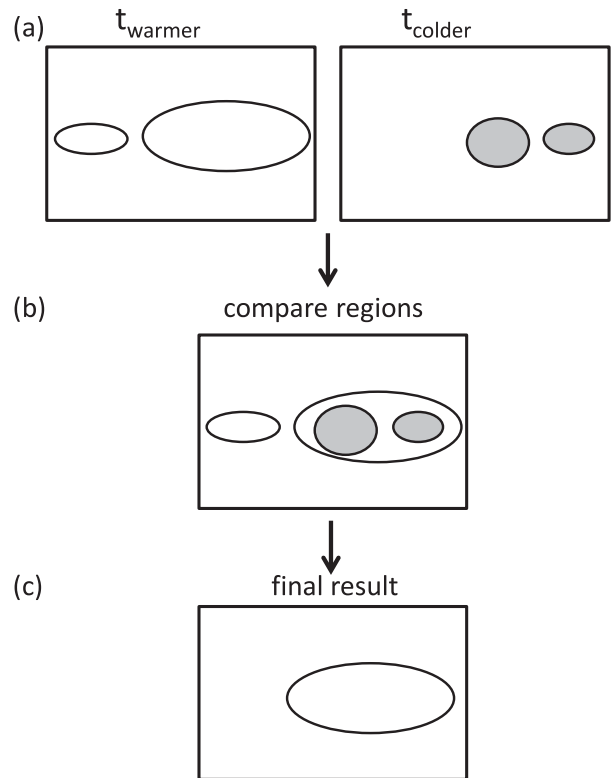


FIG. 1. Nonmax suppression thresholding technique. (a) The same field is thresholded twice at a warmer and colder OLR threshold. (b) The resulting regions are compared to identify which of the regions identified by the warmer threshold contain within them regions identified by the colder threshold and which do not. (c) Only those regions identified by the warmer threshold containing embedded regions identified by the colder threshold are retained; the others are discarded.

2008), to 150 W m^{-2} (Pearson et al. 2010, 2013; a conservatively cold cloud-top threshold chosen by those authors to minimize the risk of noncloud contamination).

A significant limitation of using a single threshold value is that it can lead to high sensitivity of the detected field to local minima and maxima. We therefore use a robust-threshold method (known in information processing as “nonmax suppression”; Canny 1986), which significantly reduces some of the sensitivity to local variations. Two OLR values are supplied: a warmer threshold and a colder threshold. The same OLR field is thresholded at each value, resulting in two separate fields of identified convection (Fig. 1a). The two resulting fields are then compared (Fig. 1b) and those regions of the field identified by the warmer threshold that contain regions of the field identified by the colder threshold are taken as convective objects (Fig. 1c). This approach thereby helps us to reduce the sensitivity of our field of identified convection to local turning points in the OLR field near the threshold value.

The robustly thresholded convective field is then divided into discrete, uniquely labeled convective objects using a four-connectivity two-pass connected components labeling (CCL) algorithm (Shapiro and Stockman 2002), which labels points sharing a common side as belonging to the same object. For each scene, the CCL output provides the total number of convective objects and area of each object. The center of mass of each object is calculated using the object areas. These in turn are used to calculate the distance between the object centers and subsequently the organization metric (described below in section 3b) for the scene. Our algorithm, written for this study, incorporates nonmax suppression and our new, fast CCL implementation. It also includes an additional “radius merge” feature not used in the current paper but documented online, as well as an option (also not used in this study) to cull small objects before the CCL part of the algorithm is run, and to use eight-connectivity labeling or higher-order clustering instead of four-connectivity. Our fast algorithm with incorporated features, along with code to calculate the convective organization potential (described in section 3b), were initially written in IDL and are now also available in Python. We make this code freely available at the following URL: https://github.com/bethanwhite/convective_organisation_ccl_idl.

An example of the output from the convective-object identification algorithm at 5 days and 19 h into the simulation (and equivalent data from GERB-SEVIRI observations) is shown in Fig. 2 alongside the OLR fields that were passed to the algorithm.

The sensitivity of the number of identified convective objects to the colder and warmer OLR thresholds was tested systematically using OLR from the Cascade models. As expected, for any given warmer threshold, the number of identified objects decreases as the colder threshold decreases (i.e., the condition for “deep” convection becomes stricter) (Fig. 3). It can also be seen that for a fixed colder threshold, decreasing the warmer threshold tends to result in more objects identified. This can be interpreted as a tendency for the cloud objects to be larger when a warmer warm threshold is used and neighboring larger objects then being more susceptible to being merged by the connectivity algorithm. After this series of tests, warmer and colder OLR thresholds of 175 and 150 W m^{-2} were chosen to be used across all datasets, consistent with the cold cloud-top threshold of 150 W m^{-2} used in the analysis of the West Africa Cascade simulations by Pearson et al. (2010, 2013), chosen to reduce the risk of noncloud contamination. Note that we choose to use absolute rather than percentile thresholds because we aim to use our technique to identify absolute differences between the datasets

and to compare our results to those already published on the Cascade data. The choice of cold thresholds is also used in the study of Roca et al. (2017), who (similarly to Pearson et al. 2010, 2013) argue that “the use of colder thresholds prevents including the whole stratiform anvil (both precipitating and nonprecipitating), while warmer thresholds can add unrelated midlevel cloudiness to the convective cluster” (p. 4286).

Finally, we note that not only can the choice of threshold pair impact the number of objects identified (Fig. 3) but also that different threshold pairs can lead to the identification of the same numbers of objects (Fig. 3) but where the morphology of the objects, and thus the diagnosed organization, may be different. We therefore perform a sensitivity test in which our input OLR datasets are also thresholded with a warmer threshold pair of 210 and 175 W m^{-2} . This choice of pair should produce a similar number of identified objects to the colder threshold pair of 175 and 150 W m^{-2} (Fig. 3). These results are shown in appendix B. We note that although the choice of threshold pair has some small impact (as to be expected) on the number of objects identified, this impact is relatively small (as may be expected through the particular choice of pair) and more importantly the temporal variability of the object numbers is unaffected. Similarly, although (as to be expected) the choice of threshold pair leads to small differences in the overall statistics of not just the object numbers but the diagnosed organization, these differences are not significant and do not change our conclusions.

b. The convective organization potential (COP)

The organization metric is constructed on the basis of an interaction potential between a set of 2D objects, where it is assumed that objects that are larger and closer together are more likely to interact with (i.e., physically influence) each other in the horizontal plane, while those that are smaller and farther apart are less likely to interact. We reduce the organization potential to 2D because of the 2D nature of many of the processes responsible for convective organization, such as gradients in SST (Zhang 1993) and surface fluxes (Tompkins and Craig 1998), convergence (Sherwood 1999) and cold pools (e.g., Fovell and Tan 1998), and because cloud size and proximity has been shown to influence the development and growth of neighboring clouds (Zhu et al. 1992). For any given scene (i.e., snapshot in time) of convective objects, three parameters are considered: the total number of objects in the scene, the size (area) of the objects, and the distance between the objects. Interaction potentials are defined between every pair of objects, and these are used to construct a single organization potential for each scene.

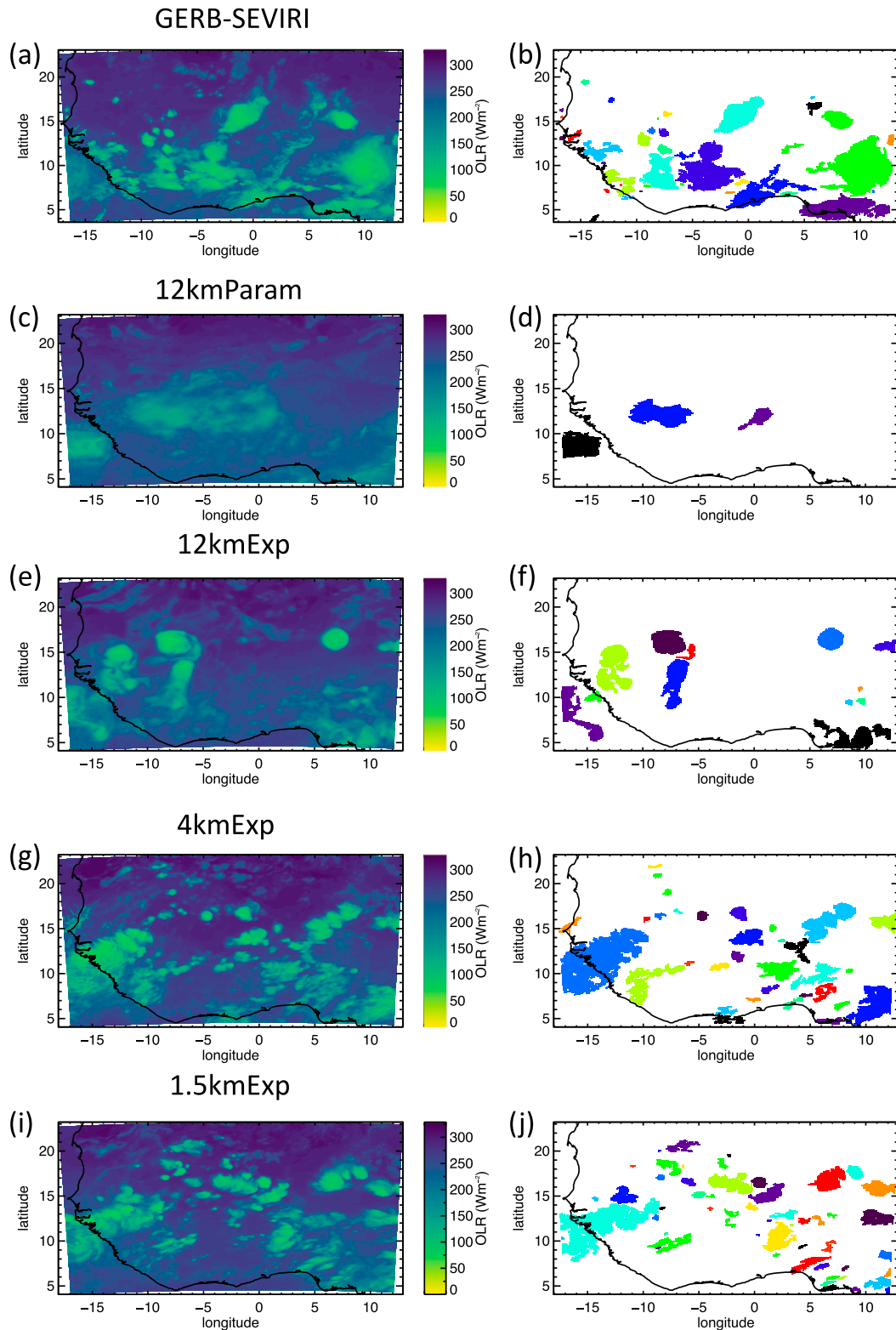


FIG. 2. (a),(c),(e),(g),(i) Instantaneous OLR ($W m^{-2}$, color scale) at 139 h into the simulation and equivalent time from the satellite observations and (b),(d),(f),(h),(j) convective objects identified in each scene at this time by the convective-object identification algorithm, for (a),(b) the satellite observations, (c),(d) 12kmParam, (e), (f) 12kmExp, (g),(h) 4kmExp, and (i),(j) 1.5kmExp. Different colors are used to represent different objects in (b), (d), (f), (h), and (j).

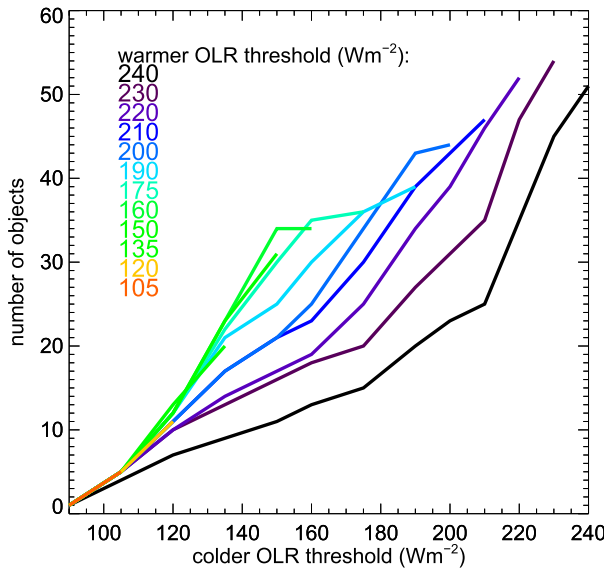


FIG. 3. Number of convective objects identified by the object-identification algorithm as a function of colder and warmer OLR thresholds (horizontal axis and colored lines, respectively). The OLR field used in this figure is from the Cascade simulation with a 12-km horizontal grid length and permitted convection.

Each scene contains a total number N of identified convective objects. Each identified convective object i has an area, A_i (known from the model grid length or satellite pixel resolution, thus giving a lower limit on object area of the square of the grid length or pixel resolution). Each object is then modeled as a circle of the same area, giving the radius of the object as $r_i = (A_i/\pi)^{1/2}$. (Note that this approximation becomes less good as objects become less round in nature). The center of the circle is at the center of mass of the original object i . For every possible pair of objects i and j in the scene, the distance $d(i, j)$ is defined between the two object centers. A dimensionless “interaction potential,” $V(i, j)$, between each pair of objects is then defined as the ratio of the sum of the object radii to the distance between the objects. Expressing this in terms of the observed or modeled quantity, the object area, gives

$$V(i, j) = \frac{\sqrt{A_i} + \sqrt{A_j}}{d(i, j)\sqrt{\pi}}. \quad (2)$$

A pair of objects therefore have an infinitely large interaction potential if they share the same center [i.e., have zero distance between them; $d(i, j) = 0$], an interaction potential of value 1 when their circumferences touch, and an interaction potential which tends to zero as the distance between them becomes infinitely large.

The interaction potentials between all possible object pairs in each scene are then combined. For N

objects in a scene, the total number of unique connections between objects is given by $\sum_{n=1}^{N-1} n = (1/2)N(N-1)$. For N objects, we define the “convective organization potential” (COP) as the sum of all the interaction potentials normalized by the total number of connections between objects:

$$\text{COP} = \frac{\sum_{i=1}^N \sum_{j=i+1}^N V(i, j)}{\frac{1}{2}N(N-1)}. \quad (3)$$

The organization potential has greater values for objects that are larger and closer together and smaller values for objects that are smaller and farther apart. The dependence of COP on the number of objects comes through changes of V with number. For a truly randomly distributed case (although not physically possible as overlap implies interaction), the organization potential is independent of number (since the small N case in a randomly distributed field of objects can be thought of as a subsample of the large N case).

Note that COP is a cloud field metric rather than a single cloud metric, and therefore in the case of a single object ($N = 1$), COP is undefined. This mathematical behavior is consistent with the notion that this metric measures the potential interaction of convective regions.

c. Comparison of COP to SCAI

Here we show that COP reproduces the same organization ranking as SCAI and thus performs well against an already known metric. Figure 4 shows both SCAI and COP calculated for the four scenes of convective objects presented in Fig. 2 of Tobin et al. (2012). SCAI ranks these four scenes from most to least ordered (lowest to highest SCAI values) as a, d, c, and b. COP also ranks these four scenes from most to least ordered (highest to lowest COP values) as Figs. 4a, 4d, 4c, and 4b. [Note that our computed values of SCAI for these grids are slightly different in value from those computed in Tobin et al. (2012), likely owing to differences in the intrinsic functions and data precision used in the analysis software used by the two sets of authors.]

While the COP metric is a new and different metric from SCAI, it also improves upon some of the disadvantages inherent to SCAI. Most importantly, unlike SCAI, COP includes consideration of the areas of convective objects. Thus, a field containing the same number of convective objects with the same centers of mass but different object sizes can have identical values of SCAI but very different values of COP. Figure 5 shows eight synthetic grids constructed to illustrate this difference between the two metrics. Each panel of Fig. 5

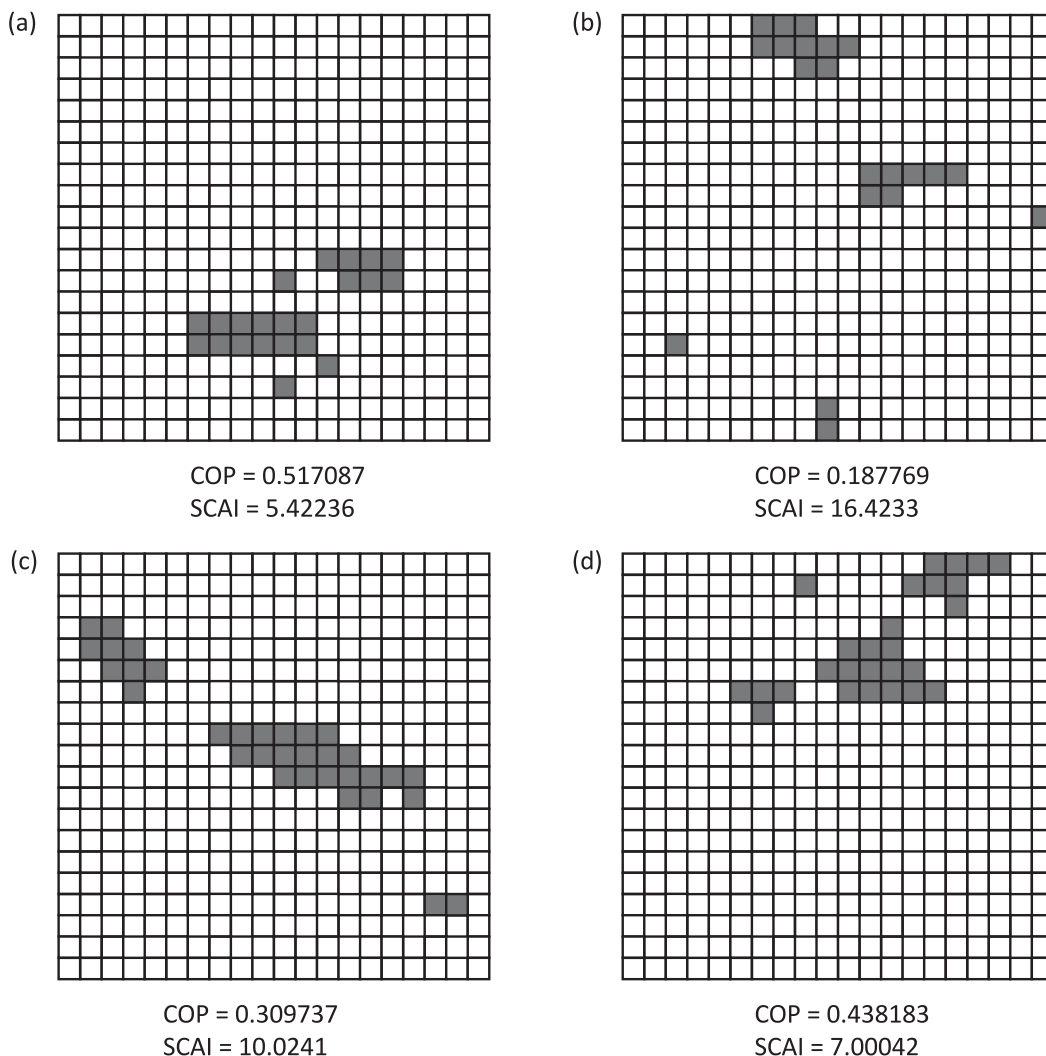


FIG. 4. SCAI and COP computed for the four grids of convective objects reproduced from Fig. 2 of Tobin et al. (2012).

contains four objects, and each of the four objects have the same centroid location in each grid. Thus, each panel of Fig. 5 has the same value of SCAI. However, because the areas of the objects vary between the grids, the value of COP varies between grids. Note also that different combinations of object areas can give rise to the same values of COP, (e.g., Figs. 5e,g and Figs. 5f,h). However, Fig. 5 shows that COP nevertheless gives a different measure of organization from SCAI. As formulated, COP most closely relates to the reciprocal of SCAI and could be interpreted as the reciprocal of an area-aware SCAI-like metric. We choose to name the metric COP because its construction takes a mathematical potential form.

Further, SCAI as originally formulated in Tobin et al. (2012), and since used in other studies (e.g., Stein et al. 2017; Holloway 2017), uses the geometric mean of the

separation distances. This can de-emphasize small distances compared to the arithmetic mean that we have decided to use for COP. While the use of the geometric mean in the calculation of SCAI may not affect the results presented in Tobin et al. (2012), it is possible that other datasets may be sensitive to these differences if SCAI is applied as formulated in Tobin et al. (2012) using only geometric mean distances.

Further still, the calculation of SCAI for a given scene of objects requires the number of objects in the scene to be normalized by the maximum possible number of objects in that scene. The calculation of SCAI also requires the geometric mean distance D_0 to be scaled by a characteristic length scale, which is quoted as 1000 km in Tobin et al. (2012) without explanation; therefore, it is not obvious how the characteristic length scale should be treated if one moves away from square domains to

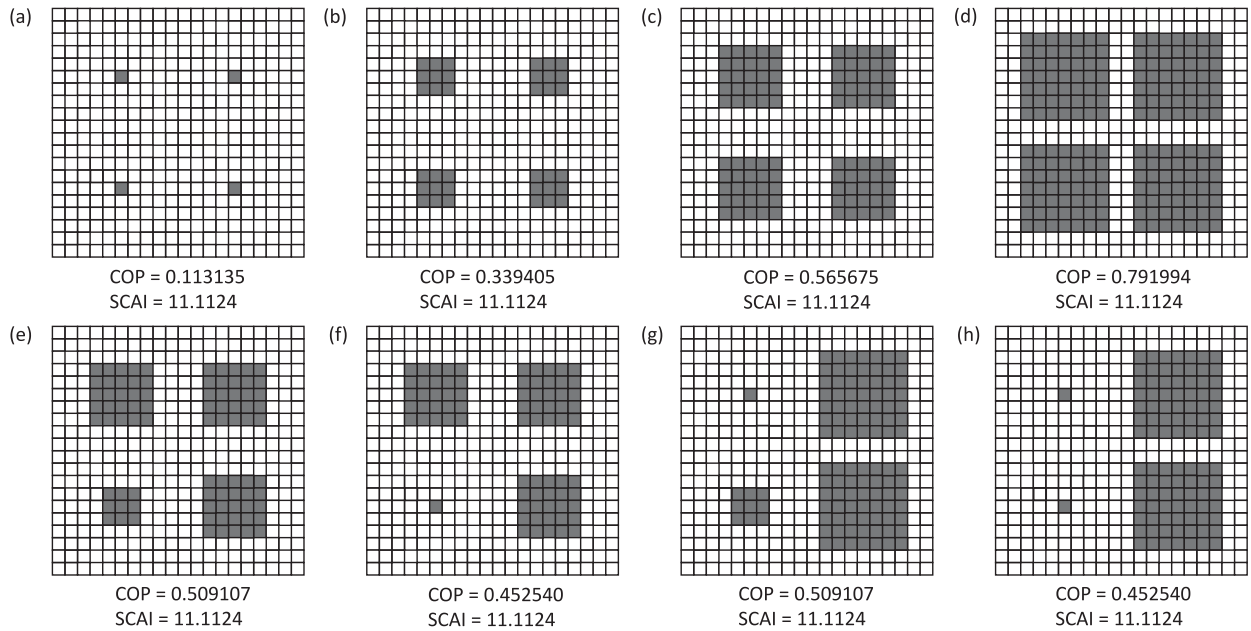


FIG. 5. Comparison of computed SCAI vs COP for synthetic fields containing the same number of objects with same object centers of masses, but different object sizes.

domains with long-channel geometry. These scaling factors mean that it is difficult to use SCAI to compare domains of significantly different sizes and resolutions or with different numbers of total possible objects. Unlike SCAI, because the interaction potential V (which forms the basis of COP) is built on the ratio of the sum of the object radii to the distance between the objects, the interaction potential V is a dimensionless quantity and therefore scale invariant. Thus, COP does not require any scaling factors to be chosen a priori and can be used to compare scenarios with different domain sizes and object numbers. For equally sized domains, each containing the same numbers of objects, with each object having the same center of mass in each domain, COP scales by a power law with the area fraction of convective objects (Fig. 6).

4. Results and discussion

It is immediately clear from Fig. 2 that the numbers, sizes, and spatial distributions of convective objects appears to depend strongly both on the model resolution and on the representation of convection. Although this could be in part due to the use of thresholds to determine regions of deep convection in the OLR data, this caveat applies to any study that uses a thresholding technique, including those of Tobin et al. (2012, 2013) and Stein et al. (2017). Our nonmaximum suppression robustly thresholding approach also makes it less likely that such sensitivities will be present in our data compared to

those studies that use a single thresholding technique (e.g., Tobin et al. 2012, 2013; Stein et al. 2017). Note that the models were not run with data assimilation and were forced only at their boundaries by ECMWF data, so the convective regions in the different models and the observations are not necessarily expected to coincide with

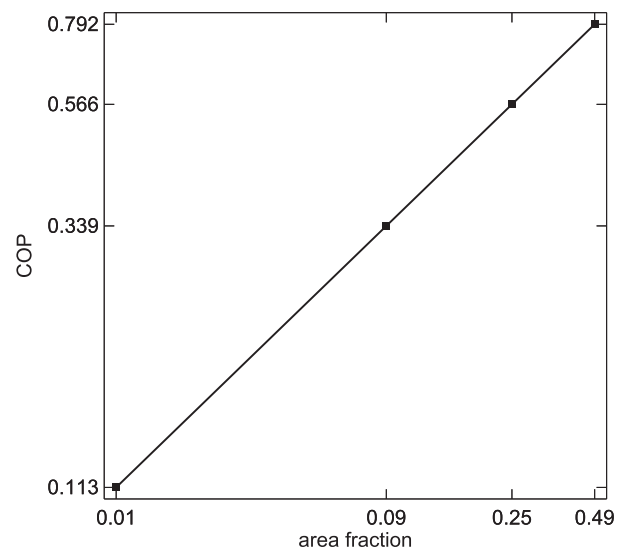


FIG. 6. The quantity $\log(\text{COP})$ as a function of $\log(\text{area fraction})$ for identically sized domains each containing the same numbers, with each object having the same center of mass in each domain, but with increasing size of each object (as in Figs. 5a–d). Area fraction for each domain is calculated as the ratio of the total area of the convective objects to the total area of the domain.

each other. Running the models in this way over a large domain allows the evolution of the domain interiors to be determined solely by the resolution and physics of each model. As such, we use the organization metrics described in section 3 to help quantify differences between the different model configurations and the observations. Specifically, we ask whether any of the model resolutions or representations of convection is best able to reproduce the observed convection.

a. Distributions of cold cloud, precipitation, and organization metrics

All models underpredict the frequency of occurrence of cold cloud compared to the GERB-SEVIRI observations (Fig. 7a). However, the 12kmParam model significantly underpredicts the frequency of all cloud colder than 150 W m^{-2} , while the permitted-convection model configurations represent cold cloud slightly better than 12kmParam compared to GERB-SEVIRI, in agreement with Pearson et al. (2010, their Fig. 2, although note their figure only shows a distribution for a single snapshot in time). Further, the higher-resolution permitted convection models (4kmExp and 1.5kmExp) improve the representation of the observed cold cloud compared to 12kmExp (Fig. 7a). However, 4kmExp reproduces the frequency of occurrence of cold cloud better compared to observations than 1.5kmExp, which underpredicts more significantly than 4kmExp, indicating limitations in the scaling of the model. It should also be noted that the permitted-convection model configurations strongly underestimate OLR values between 150 and 175 W m^{-2} compared to those observed (Fig. 7a). This suggests that although the permitted convection models do not produce enough deep cold cloud in general compared to observations (all models underpredict the frequency of occurrence of cold cloud), when they do produce deep convection the cloud tends to be too deep and too cold.

Similarly, the permitted-convection models represent the distribution of observed surface precipitation rates much better than the parameterized convection model (Fig. 7b). The 12kmParam model overpredicts low precipitation rates and significantly underpredicts high precipitation rates [in agreement with Holloway et al. (2012), although note those authors studied the Maritime Continent Cascade domain rather than the West African Cascade domain, which is the focus of the current paper]. Once the model is permitted to resolve convection, there is a tendency to overpredict the frequency of heavy precipitation rates and to underpredict light rates (Fig. 7b). This indicates possible limitations in the representation of both convective and stratiform rain production mechanisms in the model.

However, increasing model resolution leads to increasingly better representations of observed precipitation, with 12kmExp, 4kmExp, and 1.5kmExp progressively better matching TRMM-3B42 [in agreement with Holloway et al. (2012), their Fig. 2a], and 1.5kmExp performing best of all (Fig. 7b).

However, although permitted versus parameterized convection appears to be the dominant factor in determining how well the models represent cold cloud and precipitation (Figs. 7a,b), resolution appears to determine how well the models represent cloud morphology: there is a clear separation in the distribution of the number of cloud objects, with 12kmExp and 12kmParam producing fewer objects than 4kmExp, 1.5kmExp, and the GERB-SEVIRI observations (Fig. 7c). The 4kmExp model reproduces the distribution of the cloud object numbers seen in GERB-SEVIRI, while 1.5kmExp has a tendency to overpredict large numbers of objects, and the 12-km models significantly overpredict small numbers of objects and underpredict most of the range of observed object numbers (Fig. 7c).

Conversely, a combination of both model resolution and physics representation appears to contribute to how well the COP distribution is represented in the models. 12kmParam has a much broader distribution of COP values than is seen in the GERB-SEVIRI observations (Fig. 7d). The COP distribution in 12kmExp is shifted to a range that better matches that observed, although the peak COP value of the distribution is too high compared to that in GERB-SEVIRI and higher COP values are overpredicted (Fig. 7d). Increasing the model resolution to 4kmExp leads to a better representation of the observed COP distribution (Fig. 7d). However, increasing the resolution further to 1.5kmExp leads to an overprediction of low COP values compared to the GERB-SEVIRI observations (Fig. 7d). This is due to the overprediction of large numbers (Fig. 7c) of small objects (Figs. 7e,f) that tend to be much closer together (Figs. 7g,h) than those observed and indicates that progressing to ever-increasing model resolution is unlikely to be sufficient to improve the model representation of convective organization.

Because the 12-km models underpredict total numbers of objects compared to those observed and in the higher-resolution models (Fig. 7c), the frequency of occurrence of all cloud object areas is very low in 12kmParam and 12kmExp compared to GERB-SEVIRI, 4kmExp, and 1.5kmExp (Fig. 7e). However, when relative frequencies are considered it is seen that 12kmParam and 12kmExp underpredict the frequency of occurrence of small cloud objects compared to that observed in the GERB-SEVIRI observations (Fig. 7f). Further, the 4kmExp and 1.5kmExp

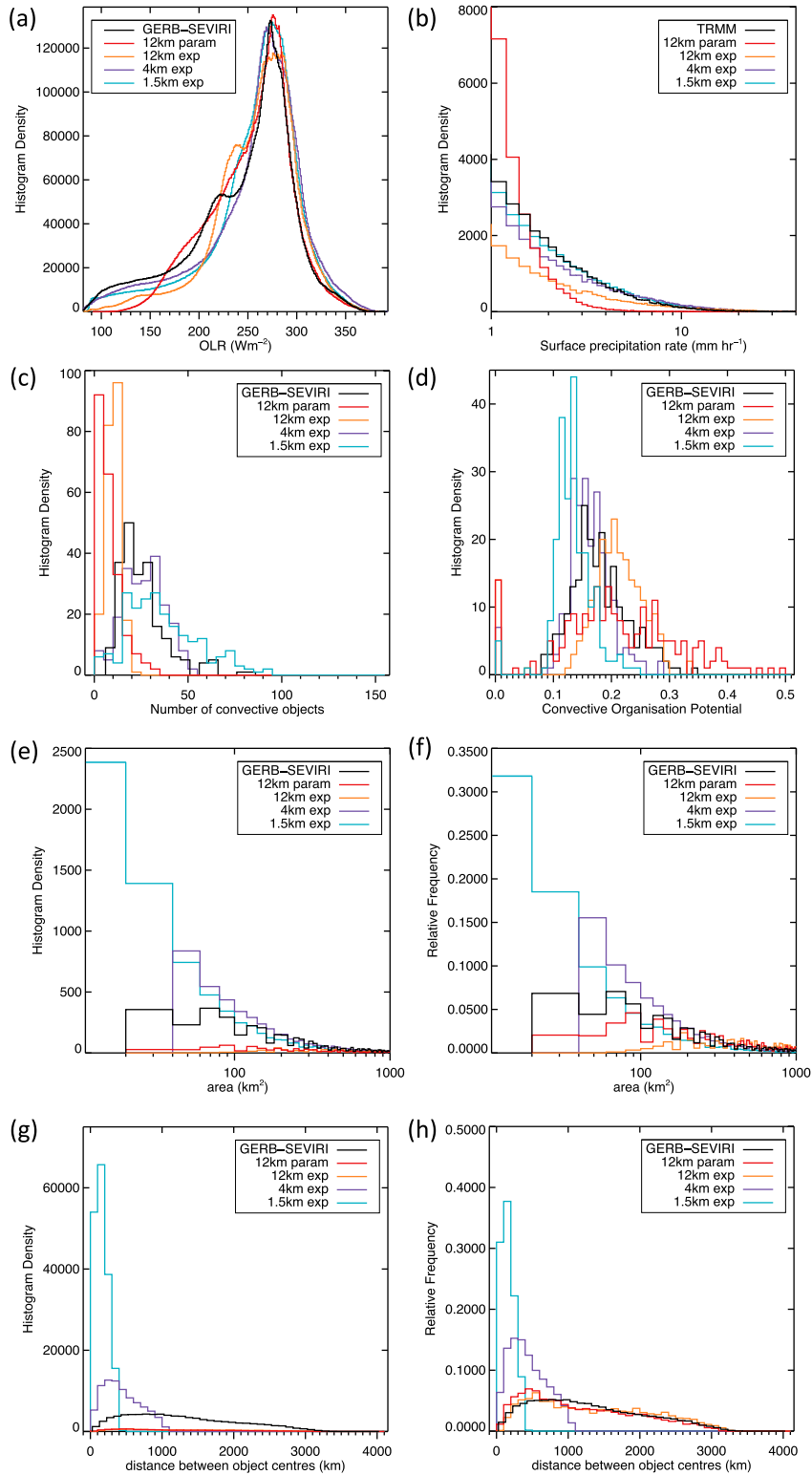


FIG. 7. Distributions of (a) OLR ($W m^{-2}$), (b) surface precipitation rate ($mm h^{-1}$), (c) number of identified convective objects, (d) convective organization potential, (e), (f) area of convective objects (km^2), and (g),(h) distance between object centers (km), for each of the model and observational datasets analyzed. Values for 12kmParam, 12kmExp,

models both overpredict the frequency of occurrence of small cloud objects, with 1.5kmExp exhibiting a large bias compared to the observations in producing clouds with an area smaller than 40 km^2 (Fig. 7f). However, both the high-resolution models perform relatively well at reproducing the observed frequency of occurrence of cloud objects larger than about 100 km^2 (Figs. 7e,f).

There are similarly large differences between the datasets in the total frequencies of occurrence of all distances between cloud objects (Fig. 7g), again owing to differences in the total numbers of objects seen between the datasets (Fig. 7a). However, when considering relative frequencies, it is seen that the 12-km models reproduce the distribution of distances between cloud objects observed in GERB-SEVIRI much better than the high-resolution models (Fig. 7h). As model resolution is increased there is a clear shift in the distribution away from the observed, with a tendency to overpredict small distances between cloud objects and underpredict large distances with increasing resolution (Fig. 7h). This is at least in part due to the overprediction of small cloud objects in 4kmExp and 1.5kmExp compared to that observed (Figs. 7e,f), as a greater number of small objects (in a fixed domain size) will lead to a greater number of small distances between those objects.

Despite differences in the abilities of the different models to represent different aspects of the cloud morphology, the higher-resolution models consistently represent the observed precipitation rates better compared to observations (Fig. 7b), perhaps indicating a decoupling between the convective organization and precipitation on time scales longer than that of an individual cloud or cloud-system life cycle. It is also interesting to note the nonlinear difference in cloud morphology between 1.5kmExp, 4kmExp, and 12kmExp despite the approximately continuous factor 3 difference between each of the model resolutions (Figs. 7c–h).

b. Behavior of organization parameters with respect to each other

To identify whether states of high and low convective organization behave differently in the different models and observations, the number of convective objects and the

mean object area are shown as a function of COP in Fig. 8, along with the number of convective objects as a function of SCAI. The 1.5kmExp model was only run for 9 days post spinup during Cascade, while the 4- and 12-km models were run for 27 days post spinup in total. In this paper, and in the rest of the Cascade literature that uses the 1.5-km model (e.g., Pearson et al. 2010; Holloway et al. 2012; Marsham et al. 2013; Stein et al. 2015), we present only data from the 9 days over which all the models were run, to avoid mixing 27-day statistics from the coarser models with 9-day statistics from the 1.5-km model. However, here we show that the behavior of the convection in the observations and 4- and 12-km models over the first 9 days (Figs. 8a,c,e) not just contains a significant number of objects but is a representative sample of the behavior over the full 27 days (Figs. 8b,d,f). Further justification that the 9-day sample is sufficient to reach a state where the results are robust enough to be representative of the performance of the model can be found in appendix A.

In general, the 12-km models have far fewer objects than the observations or the higher-resolution models or the observations (Fig. 8a), while the 4- and 1.5-km models tend to have much smaller values of COP and greater numbers of objects than the 12-km models. The lowest values of COP in the GERB-SEVIRI observations and in 4kmExp and 1.5kmExp are associated with the largest number of objects (Fig. 8a), while 12kmParam and 12kmExp exhibit a different relationship between COP and the number of objects (Fig. 8a), with a much broader range of COP values that exhibit a less clear relationship with the numbers of objects.

In comparison to COP, all models and observations show linear scaling of SCAI with the number of objects (Fig. 8b). Tobin et al. (2013) state that when objects are well distributed over the domain, the number of objects is “statistically sufficient to discriminate between the different degrees of aggregation.” The linear relationship of SCAI with number of objects in the Cascade domain similarly suggests that, for this domain and period of deep convection, SCAI does not provide more information on the organization of convection than is simply given by the number of objects. In contrast, that COP does not show linear scaling with number of objects in Fig. 8a shows that COP contains greater potential to discriminate between scenes compared to SCAI. Note also that the 12-km models have low values of

←

4kmExp, 1.5kmExp, and observations are shown in red, orange, purple, cyan, and black, respectively. Note that because of the very large differences between the absolute values present in the datasets in (e) and (g), equivalent relative frequency histograms are shown for these distributions in (f) and (h), respectively. Note in (b) the precipitation fields from the models have been coarsened to the 0.25° resolution and 3-hourly mean of the TRMM-3B42 dataset. Also note the logarithmic horizontal axes in (b), (e), and (f).

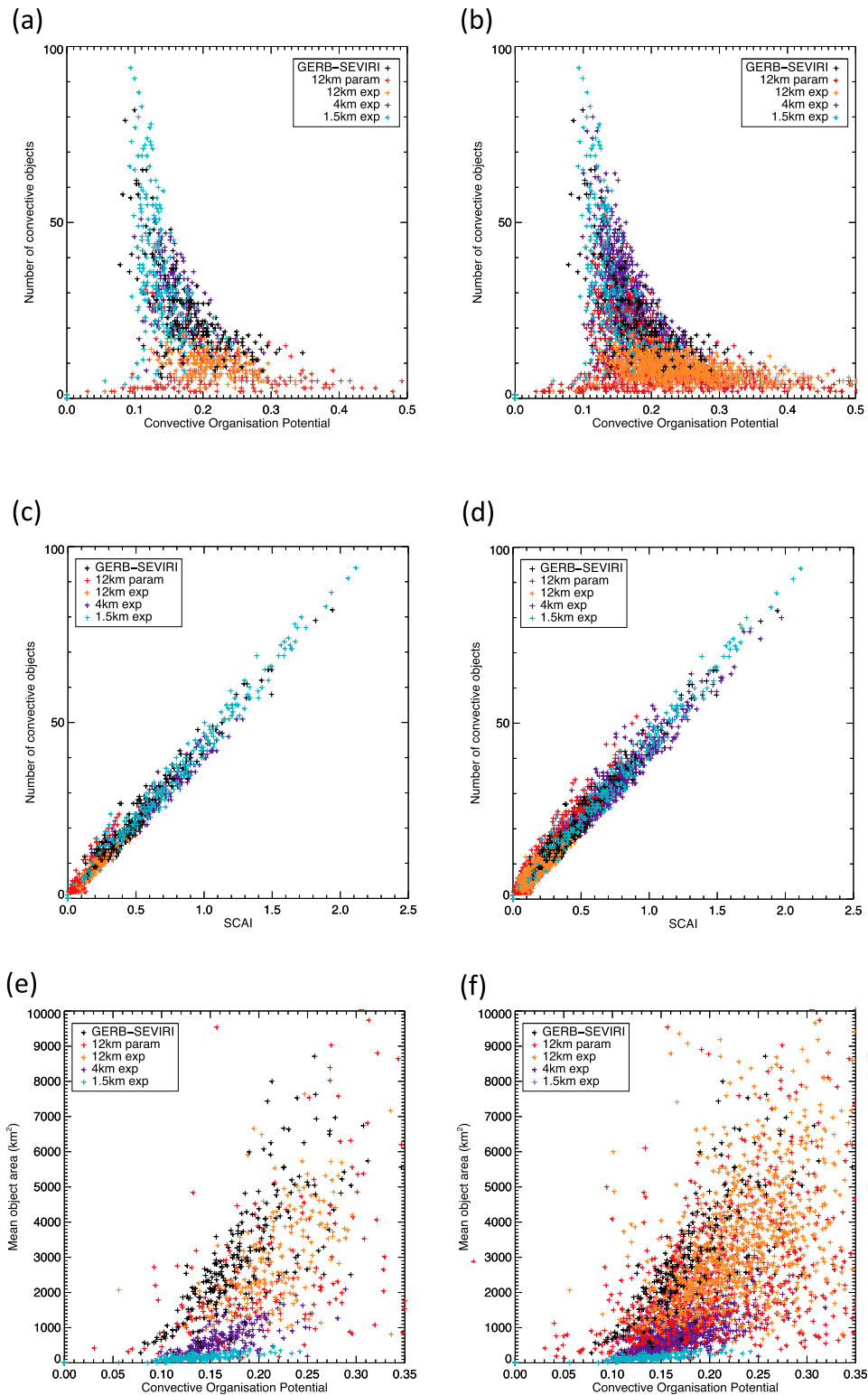


FIG. 8. Relationship of (a),(b) COP with number of convective objects, (c),(d) SCAI with number of convective objects, and (e),(f) COP with mean object area, for each of the datasets analyzed. The values for 12kmParam, 12kmExp, 4kmExp, 1.5kmExp, and GERB-SEVIRI observations are shown in red, orange, purple, cyan, and black, respectively. Data are shown for (a),(c),(e) the 9 days of the Cascade simulations used in this paper and in the rest of the Cascade literature and (b),(d),(f) the full 27 days over which the 12- and 4-km models were run.

SCAI compared to the high-resolution models and observations (Fig. 8b), while the 12-km models have higher values of COP compared to the high-resolution models and observations (Fig. 8a). Both metrics therefore indicate a greater degree of convective organization in the 12-km models than in the higher-resolution models.

Similarly, there is a clear separation of the mean area of objects associated with given values of COP between the high-resolution models and the coarser models and the observations. For a given value of COP, 4kmExp and 1.5kmExp have much smaller mean object areas than 12kmExp, 12kmParam, and the GERB-SEVIRI observations (Fig. 8e). These results show that the higher-resolution models occupy a very different organization regime than the coarser-resolution models and the observations. For example, at a COP value of 0.1, 4kmExp and 1.5kmExp have more convective objects with smaller mean areas compared to 12kmParam and 12kmExp, which have fewer but larger objects (Figs. 8a,e). Further, neither of these regimes seems to represent the observed behavior of the convection in GERB-SEVIRI, which exhibits a larger number of larger objects (Figs. 8a,e).

c. Diurnal cycles

Differences in the diurnal cycle of moist convection in West Africa have been shown to drive diurnal differences in radiation, both in net daytime heating and also in nocturnal cooling (Marshall et al. 2013). An improved representation of the diurnal cycle of tropical convection in high-resolution simulations in this region was shown by Pearson et al. (2013) to be mainly attributable to an improved representation of convection (permitted rather than parameterized convection) rather than increased model resolution per se. Indeed, a 12-km-grid-length model with permitted convection produced a more realistic magnitude of the diurnal cycle of cloud fraction compared to observations than the 4- and 1.5-km models, although the 1.5-km model produced a better match in terms of timing (Pearson et al. 2013, their Fig. 4). Comparing the diurnal cycle of the OLR from each of the models and the GERB-SEVIRI observations, 12kmParam clearly (and unsurprisingly) produces a diurnal minimum in OLR much too early (1400 LST; Fig. 9a) compared to the nocturnal minimum in cold cloud observed by GERB-SEVIRI (0200 to 0400 LST; Fig. 9a). In comparison, the permitted-convection models produce diurnal minima in cold cloud with a timing that more closely matches that observed, ranging between 0200 and 0500 LST for 12kmExp, 2300 LST for 4kmExp, and 2100 to 2300 LST for 1.5kmExp (Fig. 9a). In agreement with Pearson et al. (2013), 12kmParam produces a diurnal minimum in cold cloud too early, and the permitted-convection models represent the timing

of this minimum better compared to observations. Cold OLR values are underpredicted in the models (Fig. 7a), and thus the diurnal minima of the mean OLR values have a consistent warm bias in all models compared to GERB-SEVIRI (Fig. 9a). Despite the warm bias, the magnitude of the diurnal cycle of OLR is better represented in 4kmExp and 1.5kmExp than in 12kmExp, with low diurnal variability in mean OLR in 12kmExp compared to the high-resolution models (Fig. 9a). The diurnal cycle of OLR in 4kmExp best matches the observed magnitude, in contrast to Pearson et al. (2013), who found 12kmExp to best match observations. However, Pearson et al. (2013) analyzed the diurnal cycle of cloud fraction rather than OLR, which may explain the differences between their study and the one presented here.

Likewise, the daily maximum in mean rainfall rate in 12kmParam occurs much too early compared to that observed by TRMM [1200 LST compared to 1800 LST (Fig. 9b), in agreement with Marshall et al. (2013)]. The permitted-convection models perform significantly better in terms of timing, with 4kmExp and 1.5kmExp behaving similarly to each other in their diurnal cycles of mean surface precipitation rate (Fig. 9b), showing that the representation of convection is the leading factor in the timing of the daily rainfall peak. The timing of the daily precipitation maximum in TRMM (1800), 12kmExp (between 1800 and 2100), 4kmExp (1800), and 1.5kmExp (1500) all fall within the range of an afternoon precipitation peak between 1500 and 2100 LST observed in tracked MCSs in the Sahel (Goyens et al. 2012).

Like the diurnal cycle in OLR, where 4kmExp best matches observations (Fig. 9a), 4kmExp also performs best in the timing of the observed diurnal cycle of precipitation, whereas the daily precipitation maximum occurs too early in 1.5kmExp and too late in 12kmExp (Fig. 9b). That the delay of the daily precipitation maximum is too great in 12kmExp, represented well in 4kmExp, and not delayed enough in 1.5kmExp indicates that there may be an optimal model resolution for capturing the processes responsible for producing the precipitation maximum. This is likely related to the representation of the convective morphology: 1.5kmExp produces too many cloud objects compared to observations (Fig. 7c), which tend to be too small (Fig. 7e), whereas 12kmExp produces too few cloud objects (Fig. 7c) that do not have sufficient number of the observed midrange sizes (Fig. 7f), and 4kmExp best represents the observed cloud number and size distributions (Figs. 7c,f). Thus, it is likely that the timing of the diurnal precipitation maximum is driven by the convective organization.

Further, we note that none of the models are able to produce the secondary maximum in surface precipitation seen in TRMM at 0300 LST, indicating that

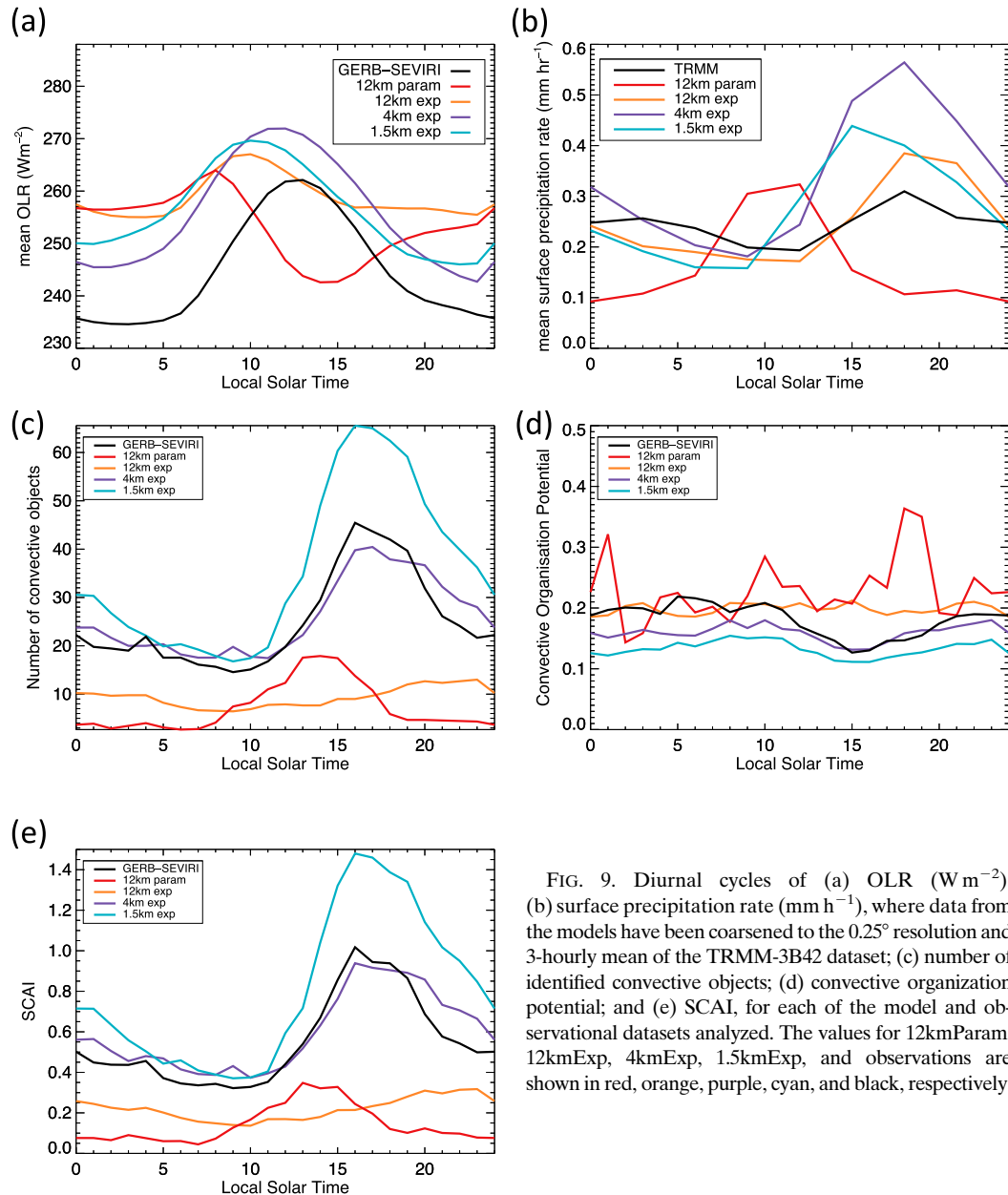


FIG. 9. Diurnal cycles of (a) OLR (W m^{-2}); (b) surface precipitation rate (mm h^{-1}), where data from the models have been coarsened to the 0.25° resolution and 3-hourly mean of the TRMM-3B42 dataset; (c) number of identified convective objects; (d) convective organization potential; and (e) SCAI, for each of the model and observational datasets analyzed. The values for 12kmParam, 12kmExp, 4kmExp, 1.5kmExp, and observations are shown in red, orange, purple, cyan, and black, respectively.

physical processes are missing from all models. Additionally, while 4kmExp best represents the timing of the daily rainfall maximum, it significantly overpredicts the magnitude of diurnal cycle and the absolute value of the maximum compared to that observed in TRMM (Fig. 9b). Indeed, all permitted convection models overpredict the magnitude of the diurnal precipitation cycle and the absolute value of the maximum, and scaling with model resolution is nonlinear, again indicating a lack of process representation in all models. These results also suggest possible underlying issues in the scaling of precipitation processes in the model and

suggest that increased model resolution alone is insufficient to improve the representation of diurnal cycles of cloud and precipitation.

As may be expected from the timing of the daily OLR minimum and precipitation rate maximum in 12kmParam, the timing of the daily maximum in number of convective objects is also too early in 12kmParam compared to the observations (Fig. 9c). The timing of the diurnal cycle of object numbers is improved in the permitted-convection models (Fig. 9c). The number of objects in 1.5kmExp varies much more strongly than in 4kmExp or 12kmExp (Fig. 9c). Although there is a large

positive bias in the diurnal cycle of object numbers in 4kmExp and 1.5kmExp compared to GERB-SEVIRI, the 12-km models underpredict the number of objects (Fig. 9c). Similarly to the representation of the timing of the daily precipitation maximum (Fig. 9b), 12kmExp underpredicts the diurnal cycle of number of objects compared to that observed, while 4kmExp well represents the observed diurnal cycle of number of objects and 1.5kmExp significantly overpredicts the number of objects during the afternoon onset of convection (Fig. 9c). This again indicates that the representation of convective organization may be responsible for how well the models predict the daily precipitation maximum (Fig. 9b). Indeed, when the diurnal cycle of COP is considered, only the 4kmExp and 1.5kmExp models reproduce the observed smoothly varying diurnal cycle, while the two 12-km models show no such smooth cycle (Fig. 9d). Although absolute values of COP in 4kmExp and 1.5kmExp are lower than those observed, the high-resolution models reproduce some of the variability of the observed diurnal cycle with a daily minimum around 1500 LST, whereas the coarse-resolution models do not (Fig. 9d).

Finally, we also show that the diurnal cycle in SCAI is almost indistinguishable from the diurnal cycle in object numbers, for all datasets considered (Fig. 9e). Thus, at least for the domain and time period considered in this study, SCAI does not appear to provide any more information about the behavior of the convective morphology than is simply given by object number [as also found by Tobin et al. (2013)], whereas the COP metric provides different and complementary information to object number.

d. Relationship of convective organization with surface winds and precipitation

Because the representation of surface precipitation appears to be linked to the degree of convective organization (Fig. 9), and because convective downdrafts are well known to produce cold pool outflow, which can in turn affect organization of convective systems (e.g., Charba 1974; Simpson 1980; Thorpe et al. 1982; Fovell and Tan 1998), we investigate whether there is any relationship between the organization parameters and the mean state of the relevant meteorological fields in the observations and the different models. For example, we seek to ask whether scenarios with a greater number of convective systems are associated with greater or weaker surface precipitation rates and whether more organized (higher COP value) scenarios are associated with stronger near-surface winds, as may be expected from a cold pool feedback hypothesis.

The mean magnitude of the 925-hPa wind and the mean surface precipitation rate are composited by the

number of convective objects and by COP (Fig. 10) in a similar manner to that of Tobin et al. (2012). Percentile bin ranges for the organization parameters are used because, unlike the decision to use absolute OLR thresholds rather than percentiles to identify convective regions earlier in this analysis, there is not yet a body of established literature on the absolute values of convective-object number or COP that may constitute highly organized versus completely isolated convection.

In all models, domain-mean near-surface winds tend to remain constant with number of convective objects up to the 4th percentile, then decrease in the states with the highest numbers of convective objects (Fig. 10a), while domain-mean surface precipitation rates are greater in states with more convective objects within the error limits shown (Fig. 10b). Greater domain-mean precipitation rates and weaker surface winds with greater numbers of convective objects may seem counterintuitive at first. However, this could be due to increased convective organization through cold pool feedbacks. Stronger surface winds (cold pool outflow) could lead to greater convective organization (smaller numbers of larger and stronger systems), where precipitation may be concentrated and enhanced within the organized systems but suppressed in a domain-mean sense due to increased subsidence. Note also that although all models tend to show an increase in surface precipitation rates with object number, this relationship is less, if at all, apparent in the TRMM observations (Fig. 10b). Yet again this indicates that all models are missing an accurate representation of the physical processes leading to precipitation in this domain.

In the permitted convection models, near-surface winds are also stronger in states with greater values of COP (Fig. 10c) (i.e., states that, on average, contain objects that are larger and/or closer together). However, near-surface winds are weaker in higher COP states in 12kmParam. This again supports the cold pool feedback hypothesis: larger convective objects produce stronger outflows, which can subsequently lead to greater convective organization. Cold pool outflow cannot be produced by the convection parameterization in 12kmParam, so it is not surprising that the relationship between COP and surface winds is different in this model from that in the permitted convection models. Note that convective organization through cold pool outflow would affect the size, number, and proximity of subsequent convection. Therefore, Figs. 10a,c could be interpreted together through a hypothesis suggesting that cold pool outflow from convective downdrafts would lead to stronger, more organized convection, seen as fewer convective objects overall (stronger winds in states with low object numbers; Fig. 10a) but that had

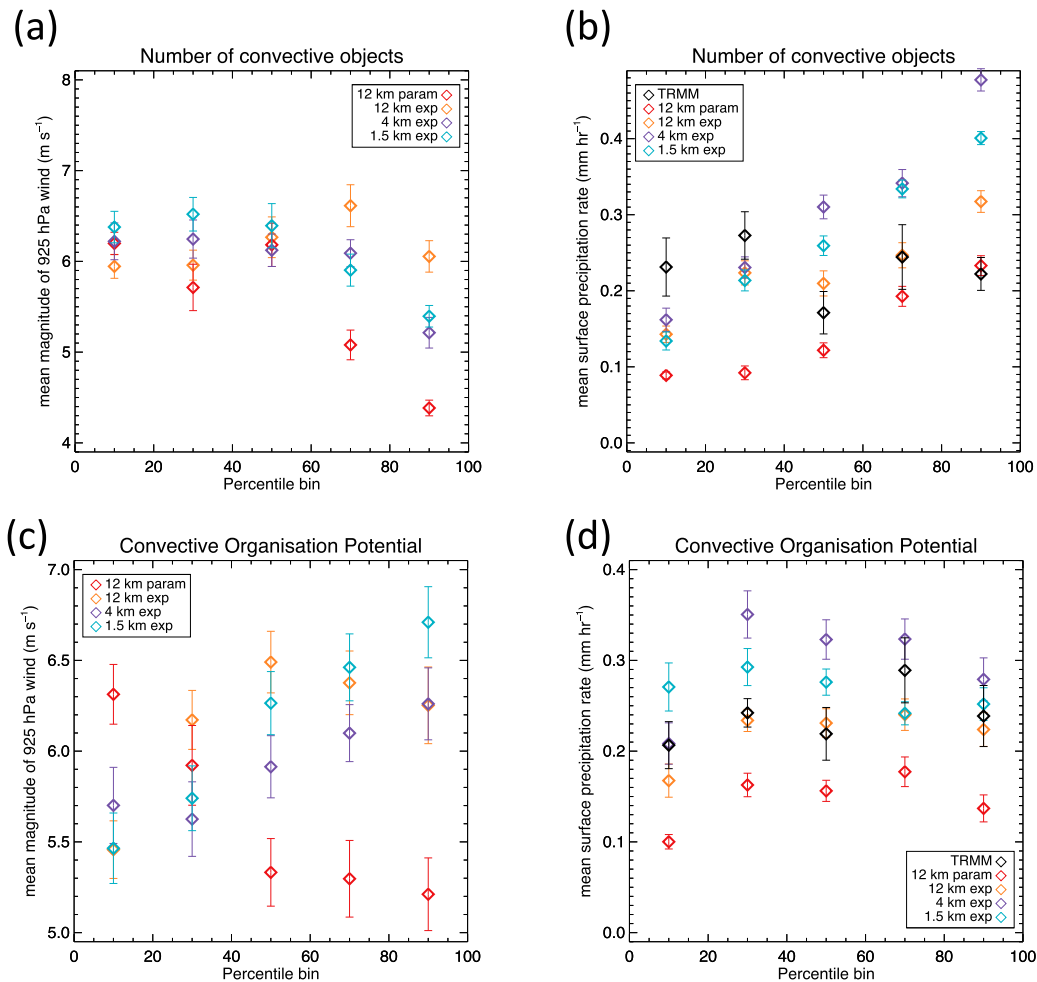


FIG. 10. (a),(c) Mean 925-hPa wind ($m s^{-1}$) and (b),(d) mean surface precipitation rate ($mm h^{-1}$), composited by percentiles of (a),(b) number of convective objects and (c),(d) convective organization potential, for each of the datasets analyzed. The values for 12kmParam, 12kmExp, 4kmExp, 1.5kmExp, and observations are shown in red, orange, purple, cyan, and black, respectively.

larger areas and tended to be closer together (stronger winds with higher COP values; Fig. 10c).

Mean surface precipitation rates increase with COP in the models and the observations, except for the highest COP states, where a tendency for decreased surface precipitation rates is seen (Fig. 10d). This again indicates that the relationship of surface precipitation rates with convective organization depends on factors other than simply the number of convective objects.

We also note that for the permitted convection model configurations, the relationship between both number of convective objects and COP with the mean 925-hPa wind speed (Figs. 10a,c) and mean surface precipitation rate (Figs. 10b,d) is very similar in 4kmExp and 1.5kmExp, while the relationships in 12kmExp differ from the two high-resolution models.

The main difference between the three permitted-convection model configurations is that the grid lengths used in the higher-resolution models are better able to resolve cloud-system processes and are at the limit or beyond the grid lengths at which it would be appropriate to use a convection parameterization. In contrast, the 12-km grid length in 12kmExp is significantly greater than that which can resolve cloud-scale processes and is within the limit at which the assumptions of traditional convection parameterizations hold. Thus, it is possible that the difference in relationships between the cloud processes and the convective organization in the higher-resolution models and the coarse-resolution convection-permitting model arise as a result of the differing abilities of the model resolutions to resolve physical processes.

5. Summary and conclusions

We have presented a method for quantifying convective organization based on the identification of convective objects and the subsequent derivation of physically motivated organization parameters. Unlike the “aggregation index” (SCAI), of [Tobin et al. \(2012\)](#), which describes a combined measure of the number of “convective clusters” and how clumped together or far apart they are, our “convective organization potential” (COP) takes the form of a physical interaction potential combining the number of convective objects, their sizes, and distance from each other. We show that COP is a different and complementary metric of convective organization from SCAI, addresses some of the disadvantages of SCAI, and can be used to discriminate states of organization that SCAI is unable to.

We have applied our metric to a set of model and observational data and shown that COP can be used to quantify differences in convective organization in models with different resolutions and physics. Unlike previous studies diagnosing convective organization in observations and models, which tend to focus on tropical oceanic convection ([Bretherton et al. 2005](#); [Tobin et al. 2012, 2013](#)), this study focuses on convection over tropical land. By applying our technique to convective objects identified from simulated and observed OLR fields we are able to quantify differences between models and observations and attribute them to differences in the model resolution or representation of convection.

Over the time periods considered, the permitted convection models produce OLR distributions more similar to those observed than the parameterized convection model [in agreement with [Pearson et al. \(2010\)](#)]. All models underpredict the frequency of occurrence of cold cloud compared to the observations, although 4kmExp and 1.5kmExp perform best compared to GERB-SEVIRI, suggesting that a second-order effect after moving from parameterized to permitted convection is that increased model resolution can improve the representation of cold cloud. However, 4kmExp performs better than 1.5kmExp, indicating either that this scaling is nonlinear or that improved representation of the cold cloud distribution with model resolution has some upper limit (which could be due to scaling issues resulting from the breakdown of assumptions made in the physics parameterizations beyond a certain grid size). The permitted convection models also produce precipitation distributions that more closely match that observed than the parameterized convection model [in agreement with [Holloway et al. \(2012\)](#)]. Precipitation distributions in the models are improved against those observed as model resolution increases, with 1.5kmExp

performing best overall, indicating that a better representation of the observed precipitation does not necessarily result in a better representation of convective cloud morphology. That neither of the high-resolution permitted convection models reproduces the observed OLR distribution best while the finest-resolution model best reproduces the observed precipitation distribution indicates there may be a decoupling between the scaling of the cloud and precipitation over time scales longer than that of one cloud system life cycle.

Model resolution dominates the degree of convective organization seen in the models. Although the COP values must be interpreted carefully owing to the fact that compensating factors may lead to the same values of COP, in general the 4kmExp model outperforms the other models in terms of representing the observed COP distribution. The 12kmExp and 12kmParam models produce too broad a range of COP values compared to that observed, while 1.5kmExp produces too narrow a range of too-small COP values. The 4kmExp and 1.5kmExp models produce, in total, more convective objects that are smaller and closer together than those in 12kmExp or 12kmParam. However, none of the models best represents the overall distribution of the observed convective morphology: although observed distributions of object numbers and COP values are best represented in 4kmExp, this model has a bias toward producing objects that are too small (a bias that worsens in 1.5kmExp), and the high-resolution models are unable to reproduce the observed distribution of distances between objects (likely resulting from the overprediction of too many small objects in these models). This indicates issues both with the ability of the model to represent the observed convective morphology and issues with the model scaling. This is in agreement with the Cascade length scale analysis of [Pearson et al. \(2013\)](#), who find that 4kmExp produces too many systems at small scales, and the results of [Stein et al. \(2015\)](#), who find that storm structures at very high resolution in another experiment are too narrow compared to those observed. However, despite the similar resolution of the GERB-SEVIRI product and the 12kmParam and 12kmExp models, the 12-km models have too few cloud objects compared to those detected in the observations (at least in part owing to the 12-km models producing less cold cloud than observed) and relatively too few small cloud objects compared to those observed. That our results agree with the finding of [Pearson et al. \(2013\)](#) that 4kmExp produces too many systems at small scales, through use of a different metric, shows that our analysis approach is detecting the same signal and is therefore a suitable alternative method.

In agreement with [Pearson et al. \(2013\)](#) and [Marshall et al. \(2013\)](#), the representation of convection is the

leading-order factor in determining how well the models represent the observed diurnal cycle of convection. The parameterized convection model misrepresents the diurnal cycle in convective cloud and precipitation, with a daily OLR minimum and precipitation maximum that occurs too early compared to that observed. Permitted convection configurations improve this, and increasing model resolution from grid lengths of 12 to 4 km in the permitted convection models leads to a better representation of the diurnal cycle of OLR and number of convective objects, but precipitation rates are over-predicted [as also found by [Holloway et al. \(2012\)](#) and [Marsham et al. \(2013\)](#)]. Further, none of the models are able to reproduce the secondary precipitation maximum seen in the observations, indicating that physical processes are missing from the models. There is no significant evidence that increasing the model grid length from 4 to 1.5 km leads to a better representation of the diurnal cycle of OLR, surface precipitation, or number of convective objects, again indicating issues with the model scaling.

Near-surface winds and surface precipitation show dependence on the degree of organization (number of convective objects and COP), indicating links between the convective organization and meteorology. However, these relationships differ somewhat between model configurations, with 12kmParam behaving least like the permitted convection models and observations. Near-surface winds are weaker and surface precipitation rates are greater in states with more convective objects. Near-surface winds are also stronger in states with larger COP values (convective objects are larger and closer together), which gives evidence for the physical motivation of the organization potential: convective organization strongly depends on secondary initiation from cold pool outflow, which in turn is associated with strong low-level winds. We suggest that these relationships could be interpreted in terms of convective organization through cold pool outflow, which would affect the size, number, and proximity of subsequent systems. Cold pool outflow from convective downdrafts could lead to stronger, more organized convection (smaller numbers of larger and stronger systems, leading to low object numbers but higher COP values), where precipitation may be concentrated and enhanced within the organized systems but suppressed in a domain-mean sense owing to increased subsidence. This surface wind increase could also be due to larger and stronger convective circulations, as seen in the later stages of self-aggregating convection (e.g., [Bretherton et al. 2005](#)). Similarly, surface precipitation rates, associated with strong evaporative cooling and the generation of cold pool outflow, tend to be higher in states with larger COP values. This again demonstrates that the

relationship of surface precipitation rates with convective organization depends on factors other than simply the number of convective objects. The cases considered in this work and those considered by [Tobin et al. \(2013\)](#) have shown that, for certain scenarios, SCAI provides no insight beyond the simple metric of convective-object number. As such, we believe more discriminating metrics would be useful for comparing and quantifying the effects of convective organization and that COP is one such metric.

Overall, we find that the organization parameters can be used to quantify differences between the models and observations. Moving from parameterized to permitted convection is in general the leading-order factor for improving model performance of the diurnal cycle and distributions of OLR and precipitation rates. Once in a permitted convection configuration, increased model resolution can lead to better model performance for some but not all aspects of the convective morphology. Improvements with increased model resolution are either non-linear or have some upper limit: despite the approximately continuous factor of 3 in resolution between grid lengths of 12, 4, and 1.5 km, there is often significant improvement in model performance between 12 and 4 km but less improvement or even decreased performance between 4 and 1.5 km. Scaling of convective cloud and precipitation processes may be decoupled. Most notably, no single model configuration “performs best” compared to observations, indicating underlying deficiencies in both the model scaling and the process understanding used to build the model. While this work has only used the organization metrics to study seasonal-scale limited-area simulations over West Africa, future work using the same metrics to study global models and observations over much longer time scales, in different climate states and different regions of synoptic meteorology, may provide results that help the development of new, physically based parameterizations of convective organization.

Acknowledgments. This research is funded from the European Research Council under the European Union’s Seventh Framework Programme (FP7/2007-2013)/ERC Grant Agreement FP7-280025 and from the European Union’s Seventh Framework Programme (FP7/2007-2013) project BACCHUS under Grant Agreement 603445. This analysis used model data from the Cascade project, which was funded by Natural Environment Research Council Grant NE/E003826/1. We thank Grenville Lister from Computer Modelling Support at the National Centre for Atmospheric Science for setting up and running the Cascade simulations. We also thank three anonymous reviewers for thoughtful comments that have greatly improved this manuscript.

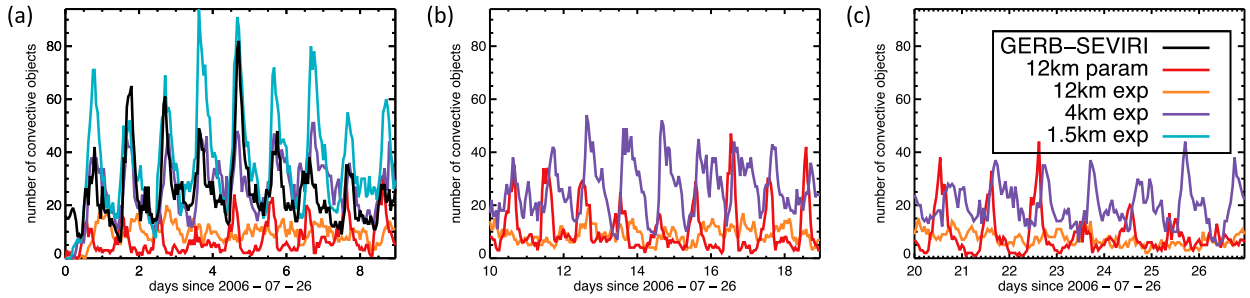


FIG. A1. Time series of the number of identified convective objects for (a) days 1–9, (b) days 10–18, and (c) days 19–27 of the Cascade period. The values for 12kmParam, 12kmExp, 4kmExp, 1.5kmExp, and observations are shown in red, orange, purple, cyan, and black, respectively. Note that 1.5kmExp was only run for days 1–9 and also that the GERB-SEVIRI observations were only available for days 1–9.

We have used precipitation observations from the Tropical Rainfall Measuring Mission (TRMM). The algorithms were developed by the TRMM Science Team. The data were processed by the TRMM Science Data and Information System (TSDIS) and the TRMM office; they are archived and distributed by the Goddard Distributed Active Archive Center. TRMM is an international project jointly sponsored by the Japan National Space Development Agency (NASDA) and the U.S. National Aeronautics and Space Administration

(NASA) Office of Earth Sciences. We have used radiance data acquired as part of the Geostationary Earth Radiation Budget Project.

APPENDIX A

Robustness of Results

We note that the 1.5kmExp model was only run for 9 days, while the coarser-resolution Cascade models

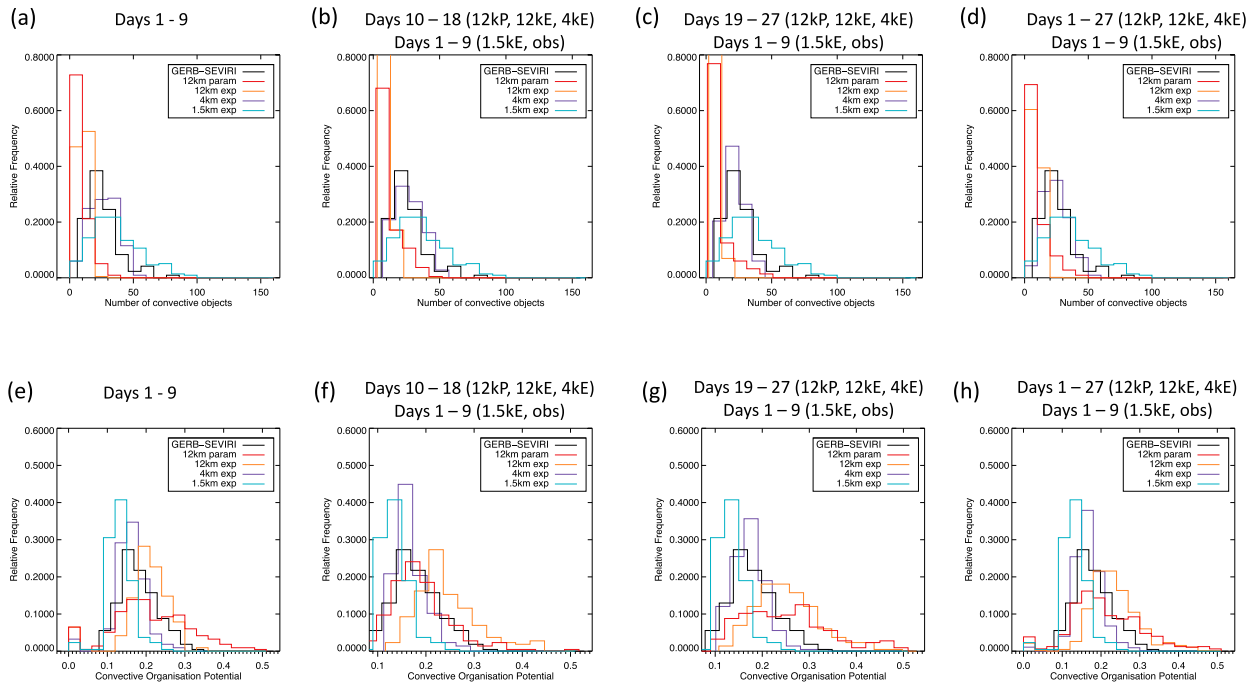


FIG. A2. Normalized distributions of (a)–(d) number of identified convective objects and (e)–(h) convective organization potential for each of the model and observational datasets analyzed over the Cascade period for (a),(e) days 1–9; (b),(f) days 10–18 for 12kmParam, 12kmExp, and 4kmExp; (c),(g) days 19–27 for 12kmParam, 12kmExp, and 4kmExp; and (d),(h) the entire available period (days 1–27 for 12kmParam, 12kmExp, and 4kmExp and days 1–9 for 1.5kmExp and GERB-SEVIRI). Note that for comparison, the distributions from days 1–9 of 1.5kmExp and GERB-SEVIRI are overlaid on the later distributions for 12kmParam, 12kmExp, and 4kmExp in (b), (f) and (c),(g). The values for 12kmParam, 12kmExp, 4kmExp, 1.5kmExp, and observations are shown in red, orange, purple, cyan, and black, respectively.

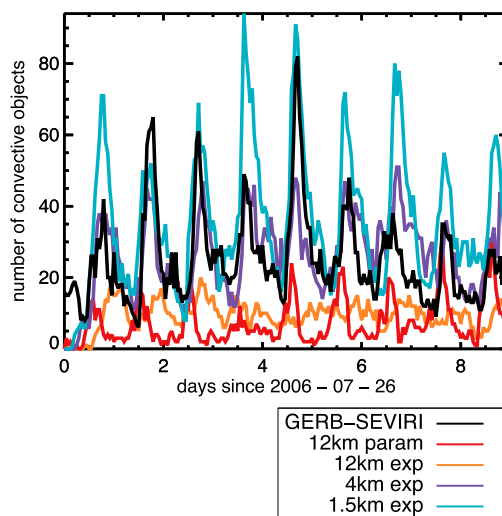
were run for 27 days. We also note that most of the literature analyzing the Cascade data uses only 9 days of simulation (e.g., Pearson et al. 2010; Holloway et al. 2012; Marsham et al. 2013; Pearson et al. 2013; Holloway et al. 2013; Stein et al. 2015). Our analysis is therefore performed over this 9-day period in order to make our results directly comparable to the other Cascade studies, and so as not to mix 9-day statistics from the observations and 1.5kmExp with 27-day statistics from 12kmParam, 12kmExp, and 4kmExp.

Nevertheless, we show here that the 9 days presented in our study are representative of the simulation period as a whole. Time series of the number of identified convective objects for days 1–9 (Fig. A1a), days 10–18 (Fig. A1b), and days 19–27 (Fig. A1c) of the Cascade period show that the number and temporal variability of convective objects occurring in the first 9 days of the simulations is similar to that occurring over the full 27 days; that is, it would appear that any subsample of the 27-day period containing more than a few diurnal cycles of convection would reasonably represent the statistics of the full period.

This is also seen when looking at the distributions of the numbers of objects and of COP. Normalized distributions sampled at 9-day subperiods of the full 27 Cascade days for object numbers (Figs. A2a–c) and COP (Figs. A2e–g) show very similar distributions of organization parameters no matter which subperiod is shown. (Note that the data from days 1–9 for 1.5kmExp and GERB-SEVIRI are overlaid onto the distributions from the coarser-resolution models at later subperiods in Figs. A2b,c,f,g for comparison). Moreover, the distributions from 12kmParam, 12kmExp, and 4kmExp composed from data from the first 9 Cascade days (Figs. A2a,e) are very similar to those composed from data over the full 27 days (Figs. A2d,h; note again that the data from 1.5kmExp and GERB-SEVIRI shown in these figures are from days 1–9), thus showing that the length of the 9-day segment used in our analysis and in most of the other Cascade studies is sufficient to reach stable statistics.

Given that the first 9-day period is sufficient to reach a state where the results are robust enough to be representative of the performance of the model, we choose to present our analysis only over this 9-day period. We emphasize again that this is in order to allow the reader to compare our results directly with those of the other Cascade papers and so as not to mix 9-day statistics with 27-day statistics, as would be the case if we presented the full datasets (27 days of 12kmParam, 12kmExp, and 4kmExp with 9 days of 1.5kmExp and GERB-SEVIRI observations).

(a) OLR thresholds: (150, 175) Wm^{-2}



(b) OLR thresholds: (175, 210) Wm^{-2}

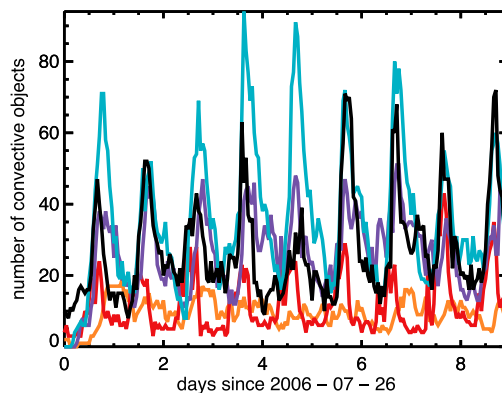


FIG. B1. Time series of the number of identified convective objects for days 1–9 of the Cascade period for objects identified using (a) the threshold pair of (150, 175) W m^{-2} presented in our study and (b) the warmer threshold pair of (175, 210) W m^{-2} performed as a sensitivity test. The values for 12kmParam, 12kmExp, 4kmExp, 1.5kmExp, and observations are shown in red, orange, purple, cyan, and black, respectively.

APPENDIX B

Sensitivity of Results to Choice of Thresholds

We note that the choice of threshold pair has a direct impact on the number of identified convective objects and also that the same number of objects (but likely with different morphologies and thus organization) can be obtained using different threshold pairs (Fig. 3). Thus we test the sensitivity of our results to the choice of threshold pair by comparing results from processing our input data with values chosen to still reasonably represent deep convection but taken as warmer values:

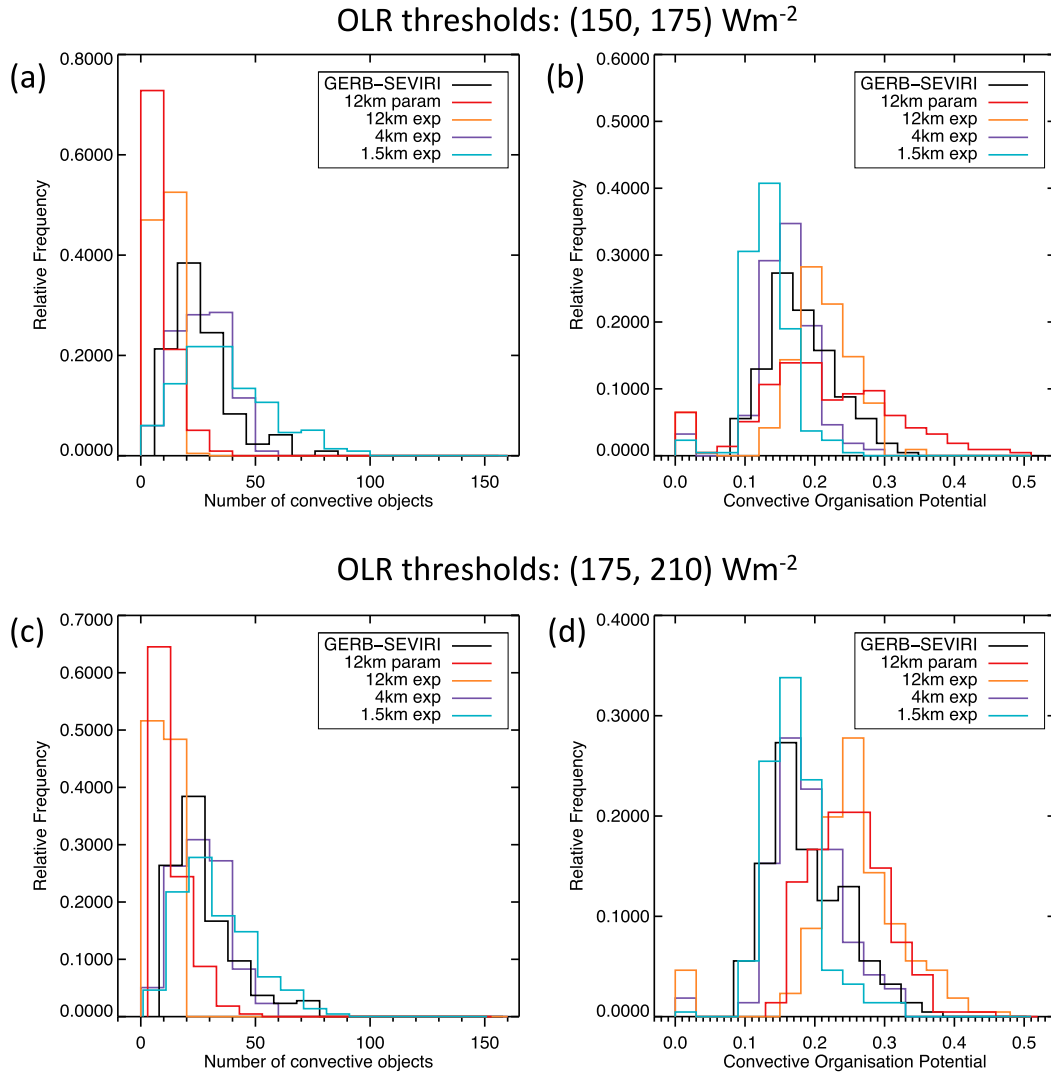


FIG. B2. Normalized distributions of (a),(c) number of identified convective objects and (b),(d) convective organization potential for each of the model and observational datasets analyzed over days 1–9 of the Cascade period, using threshold pairs of (a),(b) (150, 175) and (c),(d) (175, 210) $W m^{-2}$ to identify convective objects. The values for 12kmParam, 12kmExp, 4kmExp, 1.5kmExp, and observations are shown in red, orange, purple, cyan, and black, respectively.

175 $W m^{-2}$ for the colder threshold and 210 $W m^{-2}$ for the warmer threshold (e.g., Inoue et al. 2008). These thresholds are chosen in part to investigate the effect on the statistics when warmer cloud thresholds are chosen, but also because this particular choice of threshold pair should give rise to a similar number of objects as when the colder pair is chosen (Fig. 3) but thus with likely different morphologies.

Using the warmer cloud thresholds, we obtain time series of the number of identified convective objects over the 9-day Cascade period (Fig. B1). It can be seen that although the choice of threshold pair has

some impact (as expected) on the number of objects identified, this impact is relatively small (as may be expected through the particular choice of pair) and more importantly the temporal variability of the object numbers is unaffected by whether the colder threshold pair (Fig. B1a) or warmer threshold pair (Fig. B1b) is used. Further, it can be seen that although small differences can be seen between the distributions of number of convective objects (Figs. B2a,c) and COP (Figs. B2b,d), the overall statistics are not changed significantly when the warmer thresholds are used.

REFERENCES

- Arnold, N. P., and D. A. Randall, 2015: Global-scale convective aggregation: Implications for the Madden–Julian oscillation. *J. Adv. Model. Earth Syst.*, **7**, 1499–1518, <https://doi.org/10.1002/2015MS000498>.
- Birch, C. E., J. H. Marsham, D. J. Parker, and C. M. Taylor, 2014a: The scale dependence and structure of convergence fields preceding the initiation of deep convection. *Geophys. Res. Lett.*, **41**, 4769–4776, <https://doi.org/10.1002/2014GL060493>.
- , D. J. Parker, J. H. Marsham, D. Copsey, and L. Garcia-Carreras, 2014b: A seamless assessment of the role of convection in the water cycle of the West African monsoon. *J. Geophys. Res. Atmos.*, **119**, 2890–2912, <https://doi.org/10.1002/2013JD020887>.
- , M. J. Roberts, L. Garcia-Carreras, D. Ackerley, M. J. Reeder, A. P. Lock, and R. Schiemann, 2015: Sea-breeze dynamics and convection initiation: The influence of convective parameterization in weather and climate model biases. *J. Climate*, **28**, 8093–8108, <https://doi.org/10.1175/JCLI-D-14-00850.1>.
- Bony, S., and Coauthors, 2015: Clouds, circulation and climate sensitivity. *Nat. Geosci.*, **8**, 261–268, <https://doi.org/10.1038/ngeo2398>.
- Bretherton, C. S., P. N. Blossey, and M. Khairoutdinov, 2005: An energy-balance analysis of deep convective self-aggregation above uniform SST. *J. Atmos. Sci.*, **62**, 4273–4292, <https://doi.org/10.1175/JAS3614.1>.
- Canny, J., 1986: A computational approach to edge detection. *IEEE Trans. Pattern Anal. Mach. Intell.*, **8**, 679–698, <https://doi.org/10.1109/TPAMI.1986.4767851>.
- Charba, J., 1974: Application of gravity current model to analysis of squall-line gust front. *Mon. Wea. Rev.*, **102**, 140–156, [https://doi.org/10.1175/1520-0493\(1974\)102<0140:AOGCMT>2.0.CO;2](https://doi.org/10.1175/1520-0493(1974)102<0140:AOGCMT>2.0.CO;2).
- Coppin, D., and S. Bony, 2015: Physical mechanisms controlling the initiation of convective self-aggregation in a general circulation model. *J. Adv. Model. Earth Syst.*, **7**, 2060–2078, <https://doi.org/10.1002/2015MS000571>.
- Cotton, W., R. George, P. Wetzel, and R. McAnelly, 1983: A long-lived mesoscale convective complex. Part I: The mountain-generated component. *Mon. Wea. Rev.*, **111**, 1893–1918, [https://doi.org/10.1175/1520-0493\(1983\)111<1893:ALLMCC>2.0.CO;2](https://doi.org/10.1175/1520-0493(1983)111<1893:ALLMCC>2.0.CO;2).
- Dai, A., 2006: Precipitation characteristics in eighteen coupled climate models. *J. Climate*, **19**, 4605–4630, <https://doi.org/10.1175/JCLI3884.1>.
- , and K. E. Trenberth, 2004: The diurnal cycle and its depiction in the Community Climate System Model. *J. Climate*, **17**, 930–951, [https://doi.org/10.1175/1520-0442\(2004\)017<0930:TDCAID>2.0.CO;2](https://doi.org/10.1175/1520-0442(2004)017<0930:TDCAID>2.0.CO;2).
- Dewitte, S., L. Gonzalez, N. Clerbaux, A. Ipe, C. Bertrand, and B. de Paepe, 2008: The Geostationary Earth Radiation Budget edition 1 data processing algorithms. *Adv. Space Res.*, **41**, 1906–1913, <https://doi.org/10.1016/j.asr.2007.07.042>.
- Dirmeyer, P. A., and Coauthors, 2012: Simulating the diurnal cycle of rainfall in global climate models: Resolution versus parameterization. *Climate Dyn.*, **39**, 399–418, <https://doi.org/10.1007/s00382-011-1127-9>.
- Feng, Z., S. Hagos, A. K. Rowe, C. D. Burleyson, M. N. Martini, and S. P. de Szoeke, 2015: Mechanisms of convective cloud organization by cold pools over tropical warm ocean during the AMIE/DYNAMO field campaign. *J. Adv. Model. Earth Syst.*, **7**, 357–381, <https://doi.org/10.1002/2014MS000384>.
- Fovell, R. G., and P.-H. Tan, 1998: The temporal behavior of numerically simulated multicell-type storms. Part II: The convective cell life cycle and cell regeneration. *Mon. Wea. Rev.*, **126**, 551–577, [https://doi.org/10.1175/1520-0493\(1998\)126<0551:TTBONS>2.0.CO;2](https://doi.org/10.1175/1520-0493(1998)126<0551:TTBONS>2.0.CO;2).
- Fu, R., A. Del Genio, and W. Rossow, 1990: Behavior of deep convective clouds in the tropical Pacific deduced from ISCCP radiances. *J. Climate*, **3**, 1129–1152, [https://doi.org/10.1175/1520-0442\(1990\)003<1129:BODCCI>2.0.CO;2](https://doi.org/10.1175/1520-0442(1990)003<1129:BODCCI>2.0.CO;2).
- Futyan, J. M., and A. D. Del Genio, 2007: Deep convective system evolution over Africa and the tropical Atlantic. *J. Climate*, **20**, 5041–5060, <https://doi.org/10.1175/JCLI4297.1>.
- Goyens, C., D. Lauwaet, M. Schröder, M. Demuzere, and N. P. M. Van Lipzig, 2012: Tracking mesoscale convective systems in the Sahel: Relation between cloud parameters and precipitation. *Int. J. Climatol.*, **32**, 1921–1934, <https://doi.org/10.1002/joc.2407>.
- Grabowski, W. W., 2001: Coupling cloud processes with the large-scale dynamics using the Cloud-Resolving Convection Parameterization (CRCP). *J. Atmos. Sci.*, **58**, 978–997, [https://doi.org/10.1175/1520-0469\(2001\)058<0978:CCPWTLL>2.0.CO;2](https://doi.org/10.1175/1520-0469(2001)058<0978:CCPWTLL>2.0.CO;2).
- Guichard, F., and Coauthors, 2004: Modelling the diurnal cycle of deep precipitating convection over land with cloud-resolving models and single-column models. *Quart. J. Roy. Meteor. Soc.*, **130**, 3139–3172, <https://doi.org/10.1256/qj.03.145>.
- , and Coauthors, 2010: An intercomparison of simulated rainfall and evapotranspiration associated with a mesoscale convective system over West Africa. *Wea. Forecasting*, **25**, 37–60, <https://doi.org/10.1175/2009WAF2222250.1>.
- Guo, H., J.-C. Golaz, L. J. Donner, B. Wyman, M. Zhao, and P. Ginoux, 2015: CLUBB as a unified cloud parameterization: Opportunities and challenges. *Geophys. Res. Lett.*, **42**, 4540–4547, <https://doi.org/10.1002/2015GL063672>.
- Hanley, K. E., R. S. Plant, T. H. M. Stein, R. J. Hogan, J. C. Nicol, H. W. Lean, C. Halliwell, and P. A. Clark, 2015: Mixing-length controls on high-resolution simulations of convective storms. *Quart. J. Roy. Meteor. Soc.*, **141**, 272–284, <https://doi.org/10.1002/qj.2356>.
- Harries, J., and Coauthors, 2005: The Geostationary Earth Radiation Budget project. *Bull. Amer. Meteor. Soc.*, **86**, 945–960, <https://doi.org/10.1175/BAMS-86-7-945>.
- Held, I. M., R. S. Hemler, and V. Ramaswamy, 1993: Radiative-convective equilibrium with explicit two-dimensional moist convection. *J. Atmos. Sci.*, **50**, 3909–3927, [https://doi.org/10.1175/1520-0469\(1993\)050<3909:RCEWET>2.0.CO;2](https://doi.org/10.1175/1520-0469(1993)050<3909:RCEWET>2.0.CO;2).
- Heus, T., and A. Seifert, 2013: Automated tracking of shallow cumulus clouds in large domain, long duration large eddy simulations. *Geosci. Model Dev.*, **6**, 1261–1273, <https://doi.org/10.5194/gmd-6-1261-2013>.
- Holloway, C. E., 2017: Convective aggregation in realistic convective-scale simulations. *J. Adv. Model. Earth Syst.*, **9**, 1450–1472, <https://doi.org/10.1002/2017MS000980>.
- , S. J. Woolnough, and G. M. S. Lister, 2012: Precipitation distributions for explicit versus parameterized convection in a large-domain high-resolution tropical case study. *Quart. J. Roy. Meteor. Soc.*, **138**, 1692–1708, <https://doi.org/10.1002/qj.1903>.
- , —, and —, 2013: The effects of explicit versus parameterized convection on the MJO in a large-domain high-resolution tropical case study. Part I: Characterization of large-scale organization and propagation. *J. Atmos. Sci.*, **70**, 1342–1369, <https://doi.org/10.1175/JAS-D-12-0227.1>.

- Houze, R. A., Jr., and A. K. Betts, 1981: Convection in GATE. *Rev. Geophys. Space Phys.*, **19**, 541–576, <https://doi.org/10.1029/RG019i004p00541>.
- , M. I. Biggerstaff, S. A. Rutledge, and B. F. Smull, 1989: Interpretation of Doppler weather radar displays of midlatitude mesoscale convective systems. *Bull. Amer. Meteor. Soc.*, **70**, 608–619, [https://doi.org/10.1175/1520-0477\(1989\)070<0608:IODWRD>2.0.CO;2](https://doi.org/10.1175/1520-0477(1989)070<0608:IODWRD>2.0.CO;2).
- Huffman, G. J., and Coauthors, 2007: The TRMM Multisatellite Precipitation Analysis: Quasi-global, multiyear, combined-sensor precipitation estimates at fine scales. *J. Hydrometeorol.*, **8**, 38–55, <https://doi.org/10.1175/JHM560.1>.
- Inoue, T., M. Satoh, H. Miura, and B. Mapes, 2008: Characteristics of cloud size of deep convection simulated by a global cloud resolving model over the western tropical Pacific. *J. Meteor. Soc. Japan*, **86**, 1–15, <https://doi.org/10.2151/jmsj.86A.1>.
- Laing, A., and J. Fritsch, 1997: The global population of mesoscale convective complexes. *Quart. J. Roy. Meteor. Soc.*, **123**, 389–405, <https://doi.org/10.1002/qj.49712353807>.
- LeMone, M. A., E. J. Zipser, and S. B. Trier, 1998: The role of environmental shear and thermodynamic conditions in determining the structure and evolution of mesoscale convective systems during TOGA COARE. *J. Atmos. Sci.*, **55**, 3493–3518, [https://doi.org/10.1175/1520-0469\(1998\)055<3493:TROESA>2.0.CO;2](https://doi.org/10.1175/1520-0469(1998)055<3493:TROESA>2.0.CO;2).
- Love, B. S., A. J. Matthews, and G. M. S. Lister, 2011: The diurnal cycle of precipitation over the maritime continent in a high-resolution atmospheric model. *Quart. J. Roy. Meteor. Soc.*, **137**, 934–947, <https://doi.org/10.1002/qj.809>.
- Maddox, R., 1983: Large-scale meteorological conditions associated with midlatitude, mesoscale convective complexes. *Mon. Wea. Rev.*, **111**, 1475–1493, [https://doi.org/10.1175/1520-0493\(1983\)111<1475:LSMCAW>2.0.CO;2](https://doi.org/10.1175/1520-0493(1983)111<1475:LSMCAW>2.0.CO;2).
- Mapes, B., and R. Houze Jr., 1993: Cloud clusters and superclusters over the oceanic warm pool. *Mon. Wea. Rev.*, **121**, 1398–1415, [https://doi.org/10.1175/1520-0493\(1993\)121<1398:CCASOT>2.0.CO;2](https://doi.org/10.1175/1520-0493(1993)121<1398:CCASOT>2.0.CO;2).
- , and R. Neale, 2011: Parameterizing convective organization to escape the entrainment dilemma. *J. Adv. Model. Earth Syst.*, **3**, M06004, <https://doi.org/10.1029/2011MS000042>.
- Marshall, J. H., P. Knippertz, N. S. Dixon, D. J. Parker, and G. M. S. Lister, 2011: The importance of the representation of deep convection for modeled dust-generating winds over West Africa during summer. *Geophys. Res. Lett.*, **38**, L16803, <https://doi.org/10.1029/2011GL048368>.
- , N. S. Dixon, L. Garcia-Carreras, G. M. S. Lister, D. J. Parker, P. Knippertz, and C. E. Birch, 2013: The role of moist convection in the West African monsoon system: Insights from continental-scale convection-permitting simulations. *Geophys. Res. Lett.*, **40**, 1843–1849, <https://doi.org/10.1002/grl.50347>.
- Mauritsen, T., and B. Stevens, 2015: Missing iris effect as a possible cause of muted hydrological change and high climate sensitivity in models. *Nat. Geosci.*, **8**, 346–351, <https://doi.org/10.1038/ngeo2414>.
- Miura, H., M. Satoh, H. Tomita, A. T. Noda, T. Nasuno, and S.-i. Iga, 2007: A short-duration global cloud-resolving simulation with a realistic land and sea distribution. *Geophys. Res. Lett.*, **34**, L02804, <https://doi.org/10.1029/2006GL027448>.
- Moncrieff, M. W., and E. Klinker, 1997: Organized convective systems in the tropical western Pacific as a process in general circulation models: A TOGA COARE case-study. *Quart. J. Roy. Meteor. Soc.*, **123**, 805–827, <https://doi.org/10.1002/qj.49712354002>.
- , and C. Liu, 2006: Representing convective organization in prediction models by a hybrid strategy. *J. Atmos. Sci.*, **63**, 3404–3420, <https://doi.org/10.1175/JAS3812.1>.
- Nair, U. S., R. C. Weger, K. S. Kuo, and R. M. Welch, 1998: Clustering, randomness, and regularity in cloud fields: 5. The nature of regular cumulus cloud fields. *J. Geophys. Res.*, **103**, 11 363–11 380, <https://doi.org/10.1029/98JD00088>.
- Nesbitt, S. W., E. J. Zipser, and D. J. Cecil, 2000: A census of precipitation features in the tropics using TRMM: Radar, ice scattering, and lightning observations. *J. Climate*, **13**, 4087–4106, [https://doi.org/10.1175/1520-0442\(2000\)013<4087:ACOPFI>2.0.CO;2](https://doi.org/10.1175/1520-0442(2000)013<4087:ACOPFI>2.0.CO;2).
- Nober, F. J., and H. F. Graf, 2005: A new convective cloud field model based on principles of self-organization. *Atmos. Chem. Phys.*, **5**, 2749–2759, <https://doi.org/10.5194/acp-5-2749-2005>.
- Nolan, D. S., E. D. Rappin, and K. A. Emanuel, 2007: Tropical cyclogenesis sensitivity to environmental parameters in radiative-convective equilibrium. *Quart. J. Roy. Meteor. Soc.*, **133**, 2085–2107, <https://doi.org/10.1002/qj.170>.
- Pearson, K. J., R. J. Hogan, R. P. Allan, G. M. S. Lister, and C. E. Holloway, 2010: Evaluation of the model representation of the evolution of convective systems using satellite observations of outgoing longwave radiation. *J. Geophys. Res.*, **115**, D20206, <https://doi.org/10.1029/2010JD014265>.
- , G. M. S. Lister, C. E. Birch, R. P. Allan, R. J. Hogan, and S. J. Woolnough, 2013: Modelling the diurnal cycle of tropical convection across the ‘grey zone.’ *Quart. J. Roy. Meteor. Soc.*, **140**, 491–499, <http://doi.org/10.1002/qj.2145>.
- Pohl, B., and H. Douville, 2011: Diagnosing GCM errors over West Africa using relaxation experiments. Part II: Intraseasonal variability and African easterly waves. *Climate Dyn.*, **37**, 1313–1334, <https://doi.org/10.1007/s00382-011-1106-1>.
- Randall, D., M. Khairoutdinov, A. Arakawa, and W. Grabowski, 2003: Breaking the cloud parameterization deadlock. *Bull. Amer. Meteor. Soc.*, **84**, 1547–1564, <https://doi.org/10.1175/BAMS-84-11-1547>.
- Roca, R., and V. Ramanathan, 2000: Scale dependence of monsoonal convective systems over the Indian Ocean. *J. Climate*, **13**, 1286–1298, [https://doi.org/10.1175/1520-0442\(2000\)013<1286:SDOMCS>2.0.CO;2](https://doi.org/10.1175/1520-0442(2000)013<1286:SDOMCS>2.0.CO;2).
- , T. Fiolleau, and D. Bouniol, 2017: A simple model of the life cycle of mesoscale convective systems cloud shield in the tropics. *J. Climate*, **30**, 4283–4298, <https://doi.org/10.1175/JCLI-D-16-0556.1>.
- Rotunno, R., J. B. Klemp, and M. L. Weisman, 1988: A theory for strong, long-lived squall lines. *J. Atmos. Sci.*, **45**, 463–485, [https://doi.org/10.1175/1520-0469\(1988\)045<0463:ATFSSL>2.0.CO;2](https://doi.org/10.1175/1520-0469(1988)045<0463:ATFSSL>2.0.CO;2).
- Seifert, A., and T. Heus, 2013: Large-eddy simulation of organized precipitating trade wind cumulus clouds. *Atmos. Chem. Phys.*, **13**, 5631–5645, <https://doi.org/10.5194/acp-13-5631-2013>.
- Shapiro, L., and G. Stockman, 2002: *Computer Vision*. Prentice Hall, 608 pp.
- Sherwood, S. C., 1999: On moistening of the tropical troposphere by cirrus clouds. *J. Geophys. Res.*, **104**, 11 949–11 960, <https://doi.org/10.1029/1999JD900162>.
- Simpson, J., 1980: Downdrafts as linkages in dynamic cumulus seeding effects. *J. Appl. Meteor.*, **19**, 477–487, [https://doi.org/10.1175/1520-0450\(1980\)019<0477:DALIDC>2.0.CO;2](https://doi.org/10.1175/1520-0450(1980)019<0477:DALIDC>2.0.CO;2).
- Slingo, A., and Coauthors, 2006: Observations of the impact of a major Saharan dust storm on the atmospheric radiation balance. *Geophys. Res. Lett.*, **33**, L24817, <https://doi.org/10.1029/2006GL027869>.

- Stein, T. H. M., R. J. Hogan, K. E. Hanley, J. C. Nicol, H. W. Lean, R. S. Plant, P. A. Clark, and C. E. Halliwell, 2014: The three-dimensional morphology of simulated and observed convective storms over southern England. *Mon. Wea. Rev.*, **142**, 3264–3283, <https://doi.org/10.1175/MWR-D-13-00372.1>.
- , D. J. Parker, R. J. Hogan, C. E. Birch, C. E. Holloway, G. M. S. Lister, J. H. Marsham, and S. J. Woolnough, 2015: The representation of the West African monsoon vertical cloud structure in the Met Office Unified Model: An evaluation with CloudSat. *Quart. J. Roy. Meteor. Soc.*, **141**, 3312–3324, <https://doi.org/10.1002/qj.2614>.
- , C. E. Holloway, I. Tobin, and S. Bony, 2017: Observed relationships between cloud vertical structure and convective aggregation over tropical ocean. *J. Climate*, **30**, 2187–2207, <https://doi.org/10.1175/JCLI-D-16-0125.1>.
- Stephens, G. L., and Coauthors, 2010: Dreary state of precipitation in global models. *J. Geophys. Res.*, **115**, D24211, <https://doi.org/10.1029/2010JD014532>.
- Taylor, C. M., C. E. Birch, D. J. Parker, N. Dixon, F. Guichard, G. Nikulin, and G. M. S. Lister, 2013: Modeling soil moisture-precipitation feedback in the Sahel: Importance of spatial scale versus convective parameterization. *Geophys. Res. Lett.*, **40**, 6213–6218, <https://doi.org/10.1002/2013GL058511>.
- Thorpe, A. J., M. J. Miller, and M. W. Moncrieff, 1982: Two-dimensional convection in non-constant shear: A model of mid-latitude squall lines. *Quart. J. Roy. Meteor. Soc.*, **108**, 739–762, <https://doi.org/10.1002/qj.49710845802>.
- Tobin, I., S. Bony, and R. Roca, 2012: Observational evidence for relationships between the degree of aggregation of deep convection, water vapor, surface fluxes, and radiation. *J. Climate*, **25**, 6885–6904, <https://doi.org/10.1175/JCLI-D-11-00258.1>.
- , —, C. E. Holloway, J.-Y. Grandpeix, G. Sèze, D. Coppin, S. J. Woolnough, and R. Roca, 2013: Does convective aggregation need to be represented in cumulus parameterizations? *J. Adv. Model. Earth Syst.*, **5**, 692–703, <https://doi.org/10.1002/jame.20047>.
- Tompkins, A. M., 2001: Organization of tropical convection in low vertical wind shears: The role of water vapor. *J. Atmos. Sci.*, **58**, 529–545, [https://doi.org/10.1175/1520-0469\(2001\)058<0529:OOTCIL>2.0.CO;2](https://doi.org/10.1175/1520-0469(2001)058<0529:OOTCIL>2.0.CO;2).
- , and G. C. Craig, 1998: Radiative–convective equilibrium in a three-dimensional cloud ensemble model. *Quart. J. Roy. Meteor. Soc.*, **124**, 2073–2097, <https://doi.org/10.1002/qj.49712455013>.
- Weger, R. C., J. Lee, T. Zhu, and R. M. Welch, 1992: Clustering, randomness and regularity in cloud fields: 1. Theoretical considerations. *J. Geophys. Res.*, **97**, 20 519–20 536, <https://doi.org/10.1029/92JD02038>.
- Weisman, M. L., W. C. Skamarock, and J. B. Klemp, 1997: The resolution dependence of explicitly modeled convective systems. *Mon. Wea. Rev.*, **125**, 527–548, [https://doi.org/10.1175/1520-0493\(1997\)125<0527:TRDOEM>2.0.CO;2](https://doi.org/10.1175/1520-0493(1997)125<0527:TRDOEM>2.0.CO;2).
- Wing, A. A., and T. W. Cronin, 2016: Self-aggregation of convection in long channel geometry. *Quart. J. Roy. Meteor. Soc.*, **142**, 1–15, <https://doi.org/10.1002/qj.2628>.
- Yang, G.-Y., and J. Slingo, 2001: The diurnal cycle in the tropics. *Mon. Wea. Rev.*, **129**, 784–801, [https://doi.org/10.1175/1520-0493\(2001\)129<0784:TDCITT>2.0.CO;2](https://doi.org/10.1175/1520-0493(2001)129<0784:TDCITT>2.0.CO;2).
- Zhang, C., 1993: Large-scale variability of atmospheric deep convection in relation to sea surface temperature in the tropics. *J. Climate*, **6**, 1898–1913, [https://doi.org/10.1175/1520-0442\(1993\)006<1898:LSVOAD>2.0.CO;2](https://doi.org/10.1175/1520-0442(1993)006<1898:LSVOAD>2.0.CO;2).
- Zhu, T., J. Lee, R. C. Weger, and R. M. Welch, 1992: Clustering, randomness, and regularity in cloud fields: 2. Cumulus cloud fields. *J. Geophys. Res.*, **97**, 20 537–20 558, <https://doi.org/10.1029/92JD02022>.